International Journal of Earth Sciences

Processes and sources during Late Variscan magmatism: Inferences from mineralogy and geochemistry on the Solanas igneous complex, Sàrrabus pluton (southeastern Sardinia)

--Manuscript Draft--

Manuscript Number:	
Full Title:	Processes and sources during Late Variscan magmatism: Inferences from mineralogy and geochemistry on the Solanas igneous complex, Sàrrabus pluton (southeastern Sardinia)
Article Type:	Original Paper
Keywords:	Solanas igneous complex; mineral chemistry; geochemistry; fractional crystallisation; crustal contamination; Late Variscan intrusions
Corresponding Author:	Ciro Cucciniello Universita degli Studi di Napoli Federico II Dipartimento di Scienze della Terra dell'Ambiente e delle Risorse ITALY
Corresponding Author Secondary Information:	
Corresponding Author's Institution:	Universita degli Studi di Napoli Federico II Dipartimento di Scienze della Terra dell'Ambiente e delle Risorse
Corresponding Author's Secondary Institution:	
First Author:	Luigi Franciosi
First Author Secondary Information:	
Order of Authors:	Luigi Franciosi
	Massimo D'Antonio
	Lorenzo Fedele
	Vincenza Guarino
	Colombo C.G. Tassinari
	Roberto de Gennaro
	Ciro Cucciniello
Order of Authors Secondary Information:	
Funding Information:	Fondi Ricerca di Ateneo (DR_3450_2016) — Dr Ciro Cucciniello
Abstract:	The igneous complex of Solanas is a small, composite calc-alkaline intrusion that crops out in the Sarrabus region (southeastern Sardinia) and consists of olivine gabbronorites, amphibole gabbros, microgabbros, quartz-diorites, tonalites, plagiogranites, amphibole-granodiorites and biotite-granodiorites. The mafic rocks occur as either enclaves into quartz-diorites and tonalites, or small igneous bodies, and range in composition from primitive to relatively evolved (Mg# 70 to 49). The olivine gabbronorites and amphibole gabbros have petrographic and geochemical features consistent with a cumulate origin, and mineral chemistry similarities with island arc cumulate sequences. The microgabbros have geochemical characteristics similar to high-alumina basalts with fractionated rare earth element patterns (LaN/YbN = 4.3-6.0), enrichment in large ion lithophile elements (Ba, U, K and Pb) and depletion in Nb and Ta compared with the primitive mantle. These characteristics are consistent with magma sources involving partial melting of a mantle portion that was enriched during the subduction of oceanic crust. Mineralogy and geochemistry of the quartz-diorites-tonalites-plagiogranites-

	granodiorites suggest crystallisation from different magmas. The studied samples represent magmas that probably formed by continuous differentiation and crustal contamination of originally more mafic magmas. Field and geochemical data suggest that the Solanas intrusion results from the assembly of several melts differentiated in the middle crust prior to their emplacement. Magma mingling is the dominant physical interaction process. It is common throughout the Solanas igneous bodies, as evidenced by the presence of plagioclase xenocrysts within the microgabbros, resulting from the physical exchange of crystals between the host and the mafic magma.

Processes and sources during Late Variscan magmatism: Inferences from mineralogy and geochemistry on the Solanas igneous complex, Sàrrabus pluton (southeastern Sardinia)

Franciosi, L.[1], D'Antonio, M.[1], Fedele, L.[1], Guarino, V.[1], Tassinari, C.C.G.[2], de Gennaro, R.[1], Cucciniello, C.[1*]

1. Dipartimento di Scienze della Terra, dell'Ambiente e delle Risorse (DiSTAR), Università degli Studi di Napoli Federico II - Via Vicinale Cupa Cintia 21, 80126 Napoli (Italy)

2. Departamento de Mineralogia e Geotectônica, Universidade de São Paulo, Rua do Lago, 562, Cidade Universitária, CEP 05508–900, São Paulo, Brazil

Abstract

The igneous complex of Solanas is a small, composite calc-alkaline intrusion that crops out in the Sarrabus region (southeastern Sardinia) and consists of olivine gabbronorites, amphibole gabbros, microgabbros, quartz-diorites, tonalites, plagiogranites, amphibole-granodiorites and biotite-granodiorites. The mafic rocks occur as either enclaves into quartz-diorites and tonalites, or small igneous bodies, and range in composition from primitive to relatively evolved (Mg# 70 to 49). The olivine gabbronorites and amphibole gabbros have petrographic and geochemical features consistent with a cumulate origin, and mineral chemistry similarities with island arc cumulate sequences. The microgabbros have geochemical characteristics similar to high-

alumina basalts with fractionated rare earth element patterns (La_N/Yb_N = 4.3-6.0), enrichment in large ion lithophile elements (Ba, U, K and Pb) and depletion in Nb and Ta compared with the primitive mantle. These characteristics are consistent with magma sources involving partial melting of a mantle portion that was enriched during the subduction of oceanic crust.

Mineralogy and geochemistry of the quartz-diorites-tonalites-plagiogranites-granodiorites suggest crystallisation from different magmas. The studied samples represent magmas that probably formed by continuous differentiation and crustal contamination of originally more mafic magmas.

Field and geochemical data suggest that the Solanas intrusion results from the assembly of several melts differentiated in the middle crust prior to their emplacement. Magma mingling is the dominant physical interaction process. It is common throughout the Solanas igneous bodies, as evidenced by the presence of plagioclase xenocrysts within the microgabbros, resulting from the physical exchange of crystals between the host and the mafic magma.

Keywords: Solanas igneous complex; mineral chemistry; geochemistry; fractional crystallisation; crustal contamination; Late Variscan intrusions

* Corresponding author: ciro.cucciniello@unina.it

Introduction

The Sardinia-Corsica batholith consists of a huge amount of crust-derived calc-alkaline granitoid plutons and subordinate mantle-derived gabbroic complexes (Bralia et

al. 1982; Poli et al. 1989; Rossi and Cocherie 1991; Cocherie et al. 1994), emplaced in upper-middle crustal levels during syn to post-collisional phase of the Variscan orogeny (345-280 Ma; Cocherie et al. 2005 and references therein). Many petrological and geochemical studies emphasized the dominant role of mixing between crustal and mantle-derived melts for the origin of the Sardinia-Corsica batholith (Bralia et al. 1982; Poli et al. 1989; Zorpi et al. 1991; Cocherie et al. 1994). A key role has been attributed to magmatic differentiation (fractional crystallisation accompanied by assimilation of crustal material) only for the origin of some igneous complexes in the south-eastern sector of the Sardinia batholith (e.g. Secchi et al. 1991; Brotzu et al. 1993; Secchi and D'Antonio 1996).

The involvement of mafic magmas in the genesis and evolution of the Sardinia-Corsica batholith is testified by the occurrence of 1) (centimetre- to metre-sized) mafic microgranular enclaves hosted by the main granitoid masses, and 2) intrusive mafic bodies covering an area of a few km^2. Several studies on the magmatic microgranular enclaves (MME) of the Sardinia-Corsica batholith have shown that they resulted from mixing or mingling of mafic and crustal felsic magmas (e.g. Zorpi et al. 1989, 1991; Renna et al. 2006). Consequently, the compositions of the magmatic enclaves and of their host rock do not reflect the initial compositions of the two original components because of hybridisation processes (e.g. Zorpi et al. 1989, 1991).

The intrusive mafic bodies, cropping out in few localities of the Sardinia-Corsica batholith, can provide direct information on the type of mantle-derived inputs and constraints on the mantle sources (e.g. Tommasini and Poli 1992; Brotzu et al. 1993). The interaction between the intrusive mafic bodies and surrounding granitoid masses does not seem to have greatly affected the bulk chemical composition of the mafic complexes (e.g. Tommasini and Poli 1992). Whole-rock and

mineral compositions show that these mafic intrusions are the least evolved lithotypes of the entire Sardinia-Corsica batholith and, as such, they preserve the direct evidence for the participation of potentially mantle derived magmas in forming the voluminous Sardinia-Corsica batholith. Because of the relative rarity of mafic plutons in the Sardinia-Corsica batholith, only a few studies have been done (Zorpi et al. 1991; Tommasini and Poli 1992; Brotzu et al. 1993; Cocherie et al. 1994; Tommasini et al. 1995; Poli and Tommasini 1999).

The purpose of this study is to investigate the mafic-felsic rock association of the Solanas complex (Sàrrabus pluton, south-eastern part of Sardinia batholith), where the mafic rocks are particularly abundant and well exposed. To understand the genetic link among these rocks (which are fully described here for the first time), we carried out a detailed field, petrographic, geochemical, and isotopic study. We use petrological, chemical and isotopic data to (1) describe the systematic mineralogical and geochemical variations of the whole suite, (2) constrain the sources of the mafic rocks, (3) characterize the petrogenesis of the main rock types.

Geological setting

The Sardinia basement

Sardinia and Corsica represent a segment of the southern European Variscan chain, originated by the collision between Gondwana and Armorican plates after the consumption of Palaeotethys oceanic lithosphere (Carmignani et al. 1994; Rossi et al. 2009; Shaw and Johnston 2016). The Sardinia basement is subdivided into three structural domains (Fig. 1a), showing an increase of metamorphic grade and deformation

intensity from SW to NE (Di Simplicio et al. 1974; Franceschelli et al. 1992; Rossi et al. 2009 and references therein): 1) the Foreland zone, showing the effects of very low grade metamorphism; 2) the Nappe zone, including rock units metamorphosed to greenschist up to amphibolite facies conditions, and 3) the Inner zone, which experienced medium- to high-grade metamorphism.

The Foreland zone (i.e. the Sulcis-Iglesiente unit) consists of Cambrian to Carboniferous epicontinental, terrigenous and carbonate successions, likely belonging to the Gondwana continental passive margin (Oggiano et al. 2010), deformed and slightly metamorphosed during Visean deformation events, and forming the External fold and thrust belt (Carmignani et al. 2015). The Nappe zone (Di Pisa et al. 1992; Carmignani et al. 1994) is subdivided into External Nappes (from the Sàrrabus-Arburese unit to the Meana Sardo unit) and Internal Nappes, including the Barbagia unit (Oggiano et al. 2010; Carmignani et al. 2015). The Nappe zone units include extremely abundant volcanic products, erupted during three main magmatic cycles from the Upper Cambrian to the Ordovician-Silurian boundary (Beccaluva et al. 1981; Oggiano et al. 2010).

The Inner zone is subdivided in the Medium-grade and the High-grade metamorphic complexes, separated by the so-called “Posada-Asinara Line” suture zone (Cappelli et al. 1992). South of the Posada-Asinara Line (Baronie, Southern Anglona, Nurra, Asinara localities; Carmignani et al. 2015), the Medium-grade metamorphic complex is mainly made up of orthogneisses and metapelites of amphibolite facies, with eclogitic relics (Carmignani et al. 1994; Franceschelli et al. 2007; Cruciani et al. 2015). North of the Posada-Asinara Line (Gallura, Northern Anglona, Asinara localities), the High-grade metamorphic complex consists mainly of migmatites, and subordinately of orthogneisses

and metapelites affected by anatectic mobilization, as well as layered mafic-ultramafic bodies recrystallised under granulitic facies conditions (Rossi et al. 2009).

During the post-collisional phases, characterized by collapse and exhumation of the nappe edifice, the entire metamorphic basement was injected by calc-alkaline plutons forming the Sardinia-Corsica batholith. The plutons were emplaced between 340 and 280 Ma (Orsini 1976; Rossi and Cocherie 1991; Paquette et al. 2003; Cocherie et al. 2005; Gaggero et al. 2007) in late Variscan crustal shear zones between Gondwana and south-western Europe (Edel 1980; Matte 2001; von Raumer et al. 2012), building a broadly N-S oriented batholith discordant with the main tectonic lineaments (Fig. 1a). The earliest plutonic intrusions are represented by high Mg-K calc-alkaline granites (U1; Casini et al. 2012, 2015), emplaced in north-western Corsica between 345 and 337 Ma in a compressional regime (Rossi et al. 1988; Laporte et al. 1991; Paquette et al. 2003). A second calc-alkaline intrusive magmatic period lasted from 322 to 285 Ma (U2; Del Moro et al. 1975; Ferré and Leake 2001; Paquette et al. 2003; Oggiano et al. 2005, 2007; Gaggero et al. 2007; Casini et al. 2012), beginning with the emplacement, during the early stages of extension, of small per-aluminous granodioritic bodies in narrow strike-slip shear zones located in northern Sardinia (Oggiano et al. 2007; Gébelin et al. 2009; Casini et al. 2012). The peak of calc-alkaline plutonism occurred at 305 ± 4 Ma, emplacing voluminous monzogranitic bodies in the entire Sardinia-Corsica basement (Paquette et al. 2003). The last magmatic intrusions (U3), emplaced only in Corsica between 290 and 260 Ma, consist of alkaline granites and subvolcanic bodies (Paquette et al. 2003; Gaggero et al. 2007). Recent geological, petrological and geochronological studies (Casini et al. 2012, 2015; Musumeci et al. 2015; Cuccuru et al. 2016; Conte et al.

2017; Naitza et al. 2017) identified two main post-orogenic magmatic peaks: 1) a pre-300 Ma Old Magmatic Peak (OMP), characterized by granodioritic and monzogranitic plutons plus subordinate gabbro-tonalitic bodies, and 2) an Early Permian Younger Magmatic Peak (YMP; 290-286 Ma), with mainly monzogranitic to leucogranitic plutons.

The Sàrrabus pluton

The Sàrrabus pluton (~400 km^2) is a shallow igneous massif located in the frontal zone of the Sardinia nappe edifice (south-eastern Sardinia; Fig. 1a). It is made up of several intrusive units with high-K calc-alkaline affinity separated by sharp and discordant contacts, with late-Variscan emplacement ages roughly decreasing northward. The Sàrrabus igneous massif belongs to both main Sardinian post-collisional magmatic peaks (OMP and YMP). The OMP rocks include two main intrusive units of granodioritic to monzogranitic composition, with granodiorites cropping out mainly in the southern sector, and monzogranites cropping out to the NE. All the OMP intrusives are crosscut by small albite-rich monzosyenitic bodies (Brotzu et al. 1978; Pirinu et al. 1996) and by widespread dike swarms of both mafic and felsic composition. The YMP intrusions prevail in the northern sector of the Sàrrabus pluton, mainly represented by leucogranites belonging to three distinctive suites based on their mafic and accessory phase budget (GS1, GS2, GS3; Conte et al. 2017).

Available Rb-Sr radiometric data suggest an age of 311 ± 9 Ma for the Burcèi gabbro-tonalites, whereas the Capo Carbonara granodiorites were dated to 301 ± 3 Ma (Brotzu et al. 1993; Nicoletti et al. 1982). Peraluminous dikes in southern Sàrrabus show Rb-Sr age

of 293 ± 3 Ma (Ronca et al. 1999), while mafic dikes intruding the metamorphic basement not far from northern Sàrrabus yielded a U/Pb zircon age of 302 ± 0.2 Ma (Dack 2009).

Along the southern coastline, granodiorites typically include gabbro-tonalitic complexes of sub kilometric size near the Torre de su Fenugu, Solànas, Villasimìus (Franciosi 1999) and Capo Carbonara localities (Franciosi 1999; Poli and Tommasini 1999; Fig. 1b). The oldest intrusive body is the Burcei gabbro-tonalitic complex (Brotzu et al. 1993) cropping out in the northern part of the Sàrrabus massif. The Burcei complex is the main gabbro-tonalitic intrusion of the Sàrrabus area and of the entire Sardinian batholith. It is a composite body made up of two main intrusions of quartz-gabbroic to tonalitic composition in the southern part, and of granodioritic composition in the northern part (Brotzu et al. 1993). These igneous rocks intrude the Palaeozoic basement with sharp contacts and are dismembered by tardive monzogranites to leucogranites.

The Capo Carbonara complex was described by Poli and Tommasini (1999) as a stratified mafic body showing mechanical interaction with the surrounding granitic bodies. A more detailed investigation of the outcrop highlighted an outer massive gabbroic to tonalitic zone grading to an inner magmatic breccia between fine-grained hornblende gabbros and leucocratic tonalites, with more mafic gabbroic lithotypes cropping out along the coastline (Franciosi 1999). Similarly, in the Torre de su Fenugu gabbro-tonalitic body, fine-grained hornblende gabbros constitute a magmatic breccia dispersed into a coarse-grained matrix ranging from hornblende biotite tonalites to hornblende biotite granodiorites. Mafic fragments range from large syn-plutonic dikes to sub-elliptical, slightly flattened enclaves of decimetric size (Franciosi 1999).

The Villasimius (Campu Longu) gabbroic complex is a sub-rounded mass composed by medium- to fine-grained equigranular hornblende gabbros and tonalites including a block of coarse-grained gabbroic rocks in its inner portion. The gabbro-tonalitic rocks show a decrease of grain size at the contact with the surrounding granodiorites (Franciosi 1999).

The gabbro-tonalite-granodiorite complex cropping out in the Solanas area shows the largest variety of mafic rocks of the southern Sàrrabus. All lithotypes will be described in detail in the following paragraph.

The Solanas complex

Field and analytical work

The Solanas complex covers an area of ~0.4 km^2 (Fig. 1c). On the basis of field relationships, six igneous bodies have been recognized. Equigranular medium-grained quartz gabbros crop out to the East of Porto Murroni and toward Nord. To the East (Porto Murroni area), quartz gabbros show a decrease in grain size at the contact with strongly foliated tonalitic to quartz dioritic rocks. Olivine gabbronorites and amphibole gabbros are located along the coastline (North of Cabu Oi; Franciosi 1999; Fig. 1c). Medium-grained amphibole granodiorites crop out in the southernmost area. They show moderate magmatic foliation and are enriched in microgranular enclaves (Fig. 2a). Moving towards the contact with tonalites, the granodiorites develop a porphyroid, more leucocratic, border facies with biotite as the only mafic phase. The granodiorites occurring in the northern part are essentially biotite granodiorites.

Along the main road and towards North, the outcropping rocks are represented by

microgranular amphibole-biotite gabbros (hereafter referred to as microgabbros). The contact with tonalites and quartz diorites shows different rheological styles, being commonly quite sharp, but locally showing the evidence of mechanical interaction. The contact along the main road is characterized by a magmatic breccia (Fig. 2b) with sub-angular to slightly rounded decimetric to metric blocks of microgabbros within the tonalite. Towards the North, in the Porto Murroni area, the interaction between the two rock types results in the development of "pillow-like" structures (Fig. 2c) consisting of blobs of microgabbro within a tonalitic-quartz dioritic host rock. Large plagioclase crystals can be commonly recognized within the microgabbro blobs, giving them a sort of porphyritic-like appearance. These plagioclase crystals have the same size as those occurring in the tonalitic-quartz dioritic host (Fig. 2d). All the intrusive bodies of the Solanas gabbro-tonalitic complex, as well as the surrounding host leucocratic granodiorites, are crosscut by swarms of both mafic and felsic dikes.

Analytical techniques

The collected Solanas samples were processed and analysed for petrochemical characterization at the Dipartimento di Scienze della Terra, dell'Ambiente e delle Risorse (DiSTAR), Università degli Studi di Napoli Federico II. Samples were first cut with a diamond blade saw and then ground in a steel jaw crusher. Rock slabs were used for the preparation of rock thin sections subjected to petrographic investigations at the polarizing microscope. Modal analysis was performed on rock samples by point counting using the Leica QwinPlus software image analysis (1500 points for each thin section). Rock chips were washed in distilled water, hand-picked under a binocular microscope to remove any

231 sign of either alteration or presence of xenolithic material, and powdered in an ultrapure
232 agate mill. Four grams of rock powder for each sample (mixed with 1 ml of Polyvinyl
233 alcohol solution) were used to prepare pressed powder pellets (at 20 tons/cm^2 for 20 s),
234 analysed for major and trace elements concentrations with an Axios Panalytical X-ray
235 fluorescence (XRF) spectrometer at DiSTAR. The spectrometer is equipped with six
236 analyser crystals, three primary collimators and two detectors (flow counter and
237 scintillator), operating at different kV and mA for each analyte. Analytical uncertainties
238 are in the order of 1-2% for major elements and 5-10% for trace elements. The weight
239 loss on ignition (LOI) was obtained with standard thermogravimetric techniques, firing at
240 1000 °C small aliquots of powders pre-dried at 110 °C overnight.
241 Additional bulk-rock compositional data on a subset of samples were obtained through
242 Inductively-Coupled Optical Emission Spectrometry (ICP-OES) and Inductively-Coupled
243 Plasma Mass Spectrometry (ICP-MS) at Actlabs (Canada). Samples were mixed with a
244 flux of lithium metaborate and lithium tetraborate and fused in an induction furnace. The
245 melt was immediately poured into a solution of 5% nitric acid containing an internal
246 standard and mixed continuously until completely dissolved (~30 minutes). The samples
247 were analysed for major oxides and selected trace elements (Ba, Be, Sc, Sr, V, Y and Zr)
248 by Thermo Jarrell-Ash ENVIRO II or a Varian Vista 735 ICP optical spectrometer.
249 Calibration was performed using 7 prepared USGS and CANMET certified reference
250 materials. Fused samples were diluted and analysed by Perkin Elmer Sciex ELAN 6000,
251 6100 or 9000 ICP-MS for other trace elements (Cr, Co, Ni, Cu, Zn, Ga, Ge, As, Rb, Nb,
252 Mo, Ag, In, Sn, Sb, Cs, La, Ce, Pr, Nd, Sm, Eu, Gd, Tb, Dy, Ho, Er, Tm, Yb, Lu, Hf, Ta,
253 W, Tl, Pb, Bi, Th and U). Three blanks and five standards (three before the sample group

and two after) were analysed per group of samples. Duplicates were fused and analysed every 15 samples.

Representative analyses of the mineral phases (on polished thin sections) were obtained using a microanalysis unit equipped with an INCA X-act detector and a JEOL JSM-5310 Scanning Electron Microscope (SEM) in Energy-Dispersive Spectrometry (EDS) at DiSTAR. The standard operating conditions included a primary beam voltage of 15 kV, filament current of 50-100 μA and variable spot size from 30,000 to 200,000× magnification, 20 mm WD. Measurements were taken with an INCA X-stream pulse processor and elaborated with the Energy® software by Jeol. Energy® uses the XPP matrix correction scheme developed by Pouchou and Pichoir (1988) and the pulse pile-up correction. The quant optimization is carried out using cobalt (FWHM-full width at half maximum peak height-of the strobed zero = 60–65 eV). The following standards were used for calibration: diopside (Ca), San Carlos olivine (Mg), anorthoclase (Al, Si), albite (Na), rutile (Ti), fayalite (Fe), Cr_2O_3 (Cr), rhodonite (Mn), orthoclase (K), apatite (P), fluorite (F), barite (Ba), strontianite (Sr), zircon (Zr, Hf), synthetic Smithsonian orthophosphates (REE, Y, Sc), pure vanadium, niobium and tantalum (V, Nb, Ta), Corning glass (Th and U), sphalerite (S, Zn), galena (Pb), sodium chloride (Cl) and pollucite (Cs). The Kα, Lα, or Mα lines were used for calibration, according to the element. Backscattered electron (BSE) images were obtained with the same instrument.

Whole-rock Sr and Nd isotope analyses were determined at the Geochronological Research Center of the University of São Paulo using conventional ion exchange chromatography combined with thermal ionization mass spectrometry (TIMS) following the analytical procedures published in Souza (2009) and Petronilho (2009). The Sr and

Nd isotope ratios were normalized to $^{86}Sr/^{88}Sr$ = 0.1194 and $^{146}Nd/^{144}Nd$ = 0.7219, respectively, for in-run isotopic fractionation correction. The blanks for Sr are 110 pg. The banks for Nd are 150 pg. The accuracy of measurements was checked against the NBS987 standard for Sr isotopic ratios ($^{87}Sr/^{86}Sr$ = 0.710236±0.000020, n = 20), and JNdi-1 standard for Nd isotopic ratios ($^{143}Nd/^{144}Nd$ = 0.512090±0.000008, n = 24).

Results

Petrography

The igneous rock samples of this study were collected from the best exposures of representative igneous bodies and facies of the Solanas complex. On the basis of petrography and modal classification (Streckeisen 1976; Fig. 3), the Solanas rocks are classified as olivine gabbronorites (oGb), amphibole gabbros (aGb), microgabbros (mGb), quartz diorites (QD), tonalites (TN), plagiogranites (plG), amphibole-granodiorites (aGd) and biotite-granodiorites (btGd). The main textural and mineralogical features of each rock type are described below (and briefly summarized in supplementary Table S1).

The quartz gabbros (described in section 3; Fig. 1c) have been excluded from this study because of their deep alteration status.

Olivine gabbronorites (oGb; GLR33,34,36, L45,46) are medium-grained rocks mainly consisting of plagioclase, olivine, clinopyroxene, amphibole, orthopyroxene and rare interstitial brown mica (sample L45). Apatite and pyrite are common accessory phases and occur as small grains enclosed in amphibole crystals. Chromium-rich spinel occurs as inclusions in olivine. Plagioclase (modal abundances ~40-45 vol.%) occurs generally as

300 randomly-oriented euhedral to subhedral lath-shaped cumulus crystals varying from ~0.5
301 to ~2.5 mm in length. Olivine (~15 vol%) occurs as cumulus grains, generally altered to
302 iddingsite along fracture surfaces. Clinopyroxene (~15-20 vol%) occurs as subhedral to
303 anhedral crystals, varying from ~0.5 to ~2 mm in width. In sample GLR36, relics of
304 clinopyroxene are enclosed in pale green to brownish amphibole grains. Amphibole (~10-
305 15 vol%) occurs generally as large oikocrysts enclosing small plagioclase, pyroxene and
306 olivine crystals (Fig. 4a). Orthopyroxene (~15 vol%) occurs as subhedral to anhedral
307 crystals and sometimes poikilitically enclosing olivine grains. The crystallisation
308 sequence that led to development of olivine gabbronorite rocks can be inferred as
309 follows: olivine → plagioclase → clinopyroxene + orthopyroxene → amphibole.
310 Many oGb samples are visibly altered in hand specimen and under the microscope.
311 Crystals of olivine, plagioclase, pyroxene and amphibole appear partially or completely
312 replaced by serpentine, albite, clinozoisite, epidote, chlorite and secondary amphibole.
313 *Amphibole gabbros* (aGb; GLR35,37,38, L44,47) are medium-grained rocks, and
314 consist mainly of plagioclase and amphibole. Plagioclase (~60 vol%) occurs mainly as
315 large euhedral to subhedral cumulus crystals showing a peculiar internal structure with
316 complex zoning (Fig. 4b; supplementary Fig. S1) and occasionally enclosing small pale
317 green amphiboles, whereas small plagioclase grains are in turn enclosed by large
318 amphibole crystals. Amphibole (~40 vol%) is mainly subhedral and weakly coloured in
319 thin section, less commonly displaying anhedral habitus and enclosing small plagioclase
320 grains. Clinopyroxene occurs only as relics in large amphibole crystals, showing a
321 characteristic sieve-like texture in which, the resorbed zones are filled with amphibole.
322 Quartz (<5 vol%) is anhedral and occupies the interstices between plagioclase and

amphibole grains, suggesting late crystallisation. Accessory minerals include apatite, mica, pyrite, titanite and zircon. Hydrothermal alteration has been locally intense, converting primary amphibole to mixtures of secondary amphiboles, and plagioclase to clinozoisite and epidote.

Microgabbros (mGb; L7,8,10,11,12,30,31,53,71) are fine-grained rocks with hypidiomorphic texture (Fig. 4c) consisting of plagioclase (~40 vol%), amphibole (~35 vol%), biotite (15-20 vol%) and small amounts of quartz (5 vol%). Elongated crystals (mainly plagioclase and amphibole) are occasionally iso-oriented, defining a fluidal texture. Plagioclase crystals are euhedral to subhedral and mainly show elongated habitus. Amphibole occurs as euhedral to subhedral green crystals, sometimes showing a pale-coloured core. Biotite crystals are subhedral to anhedral and typically interstitial between plagioclase and amphibole. Quartz is always anhedral and occurs in interstitial position. Accessory phases are opaque oxides (mainly as inclusions in amphiboles), acicular apatite (in plagioclase) and rare zircons. The inferred crystallisation sequence is plagioclase → plagioclase + amphibole → biotite → quartz.

As previously mentioned in the field description section, mGb develop a porphyritic-like texture close to the contact with dioritic-tonalitic rocks. In thin section, the "porphyritic" samples show large crystals of plagioclase, some of which displaying patch-zoned texture (Fig. 4d; supplementary Fig. S1) and, in minor amounts, of biotite and hornblende.

Quartz-diorites (QD; GLR16, L14,57,70) *and tonalites* (TN: GLR42, L15,28,32,33,51,79,80,91) are medium-grained rocks with hypidiomorphic texture made up of plagioclase, amphibole, biotite and quartz. They are petrographically very similar to

each other, differing only for the modes of quartz and amphibole, and for the occurrence of small amount of clinopyroxene and orthopyroxene in some QD (L57,70). It is noteworthy that the samples classified as QD are those collected closer to the contact with mGb. Plagioclase (50-60 vol%) occurs mainly as large laths, similar to those observed in the "porphyritic" microgabbros. Patchy zoned plagioclase grains also occur. Amphibole (15-20 vol%) is rarely represented by euhedral crystals, more frequently occurring as subhedral to anhedral crystals often enclosing biotite and apatite grains (Fig. 4e). The biotite (10-15 vol%) occurs mainly as subhedral to anhedral crystals and, more rarely, as interstitial phase. Anhedral quartz (10-20 vol%) is always in interstitial position. Minor amounts of anhedral alkali feldspar are locally present. Accessory minerals are represented by apatite, ubiquitously included in all the observed main phases, and zircon inclusions in plagioclase and biotite. Titanite, ilmenite and epidote are more frequent in the tonalite rocks. In the northern area of the Solanas complex, tonalites with microgranular texture (e.g. L28) have been also observed. The crystallisation sequence can be inferred as: plagioclase → plagioclase + amphibole → amphibole + biotite → biotite → quartz.

Plagiogranites (Trondhjemites, plG; L16,55) are holocrystalline, medium-grained with a hypidiomorphic-heterogranular texture made up of plagioclase, quartz, biotite, rare amphibole and orthopyroxene (Fig. 4f). As in QD and TN, plagioclase (~50 vol%) occurs as large fractured laths, as well as in smaller euhedral to subhedral crystals. Quartz is more abundant (~30 vol%) than in tonalites and is represented by large anhedral crystals and small interstitial grains. Quartz is also observed in the fractures of plagioclase laths. Mafic minerals do not exceed 15 vol% and are mainly represented by biotite, occurring

as subhedral to anhedral plates that often form clusters with accessory anhedral orthopyroxene (<5 vol%). Amphibole is very rare and occurs exclusively around the edges of orthopyroxene crystals. Accessory minerals include small apatite grains and opaque oxides included in the mafic phases.

Amphibole-granodiorites (aGd; GRL32,41, L13,52,54) are hypidiomorphic, rarely (weakly) porphyroid, medium-grained rocks consisting of plagioclase, quartz, alkali feldspar, amphibole and biotite (Fig. 4g). Plagioclase (~45 vol%) occurs as slightly zoned euhedral to subhedral crystals. In the porphyroid samples, fractured laths of plagioclase similar to those of tonalitic rocks, are occasionally observed. Alkali feldspar (~15 vol%) is represented by subhedral microcline crystals, rarely occurring as an interstitial phase together with quartz. The latter (25-30 vol%) is typically anhedral and often occupies the interstices between plagioclase laths. Mafic minerals make up about 10-15 vol.% of the rock, mainly consisting of subhedral green amphibole crystals, occasionally forming cluster with biotite. A leucocratic border-facies is also observed in the main granodioritic outcrop (i.e. sample L81), consisting of an amphibole-free heterogranular rock with alkali feldspar contents up to 25 vol%, very similar to the host biotite-granodiorite (see below). The main accessory minerals of aGd are apatite, zircon, ilmenite and minor titanite, typically observed in the mafic clusters. The inferred crystallisation sequence is: plagioclase + amphibole → amphibole + biotite → alkali-feldspar → quartz.

Biotite-granodiorites (btGd; GRL10, L27,81) are heterogranular hypidiomorphic rocks made up of plagioclase, quartz, alkali-feldspar and biotite (Fig. 4h). Very rare amphibole does not exceed 2% by volume. Plagioclase (~35 vol%) occurs as euhedral to subhedral unzoned crystals. Alkali feldspar (20 vol.%) occurs as subhedral to anhedral

microcline crystals, occasionally crystallised in interstitial position together with quartz. The latter (~35 vol%) is represented by anhedral crystals of variable size. Biotite is always subhedral to anhedral and never exceeds 10 vol.%. Common accessory minerals are apatite, titanite and zircon, both as small inclusion in biotite crystals. The inferred crystallisation sequence is: plagioclase → biotite → alkali feldspar → quartz.

Mineral chemistry

Olivine occurs only in the fresh oGb (e.g. samples GLR36 and L45). The forsterite content ranges from Fo_{68} to Fo_{75} [Fo = Mg*100/(Mg+Fe); supplementary Table S2; Fig. 5a]. The MnO ranges from below detection limits (b.d.l.) to 0.013 apfu (atoms per formula unit), whereas NiO is highly variable and ranges from below detection limit to 0.012 apfu.

Orthopyroxene in the oGb shows a restricted range of composition from $Ca_1Mg_{75}Fe_{24}$ to $Ca_3Mg_{68}Fe_{29}$ [Mg# = 70-76, where Mg# = 100*Mg/(Mg+Fe); supplementary Table S3; Fig. 5b]. The Al_2O_3 and MnO contents range up to 0.106 apfu and 0.017 apfu, respectively. Cr_2O_3 content is low (<0.007 apfu). Ca-poor pyroxene ($Ca_{3-10}Mg_{37-46}Fe_{50-59}$; Mg# = 38-48) is present also in the QD (L57, L70) and plG (L55), displaying Al_2O_3 contents of 0.086-0.173 apfu.

The orthopyroxene in Solanas oGb has higher Mg# (70-76) with respect to the orthopyroxene found in the Burcei gabbro-tonalites (Mg# = 66-50; Brotzu et al. 1993). Few corroded cores and xenocrysts observed in the Burcei gabbro-tonalites display higher Mg# (78-88; Fig. 5b).

Clinopyroxene in the oGb is diopside and Ca-rich augite ($Ca_{40-48}Mg_{43-47}Fe_{9-13}$) (supplementary Table S3; Fig. 5b). Al_2O_3 content ranges widely from 0.031 apfu to 0.213 apfu. TiO_2 content ranges from b.d.l. to 0.021 apfu. Clinopyroxenes from aGb are diopside ($Ca_{47-49}Mg_{38-41}Fe_{12-13}$) (supplementary Table S3; Fig. 5b). They contain low Al_2O_3 (0.027-0.059 apfu) and TiO_2 (up to 0.007 apfu) concentrations, respectively. Clinopyroxenes of the oGb have higher Mg# (78-86) than clinopyroxenes of aGb (Mg# = 75-78) and Burcei gabbro-tonalites (Mg# = 54-64; Fig. 5b).

Spinel occurs as inclusions in the olivine of the oGb. Two kinds of spinels have been observed: (1) magmatic Al-spinels (Al_2O_3 = 6.593-8.945 apfu; Cr_2O_3 = 4.688-5.263 apfu; supplementary Table S4), and (2) hydrothermally altered "ferritic-chromitic" spinels (Al_2O_3 = 0.255-1.432 apfu; Cr_2O_3 = 4.067-5.289 apfu; supplementary Table S4).

Fe-Ti oxides are relatively rare in Solanas rocks, never exceeding accessory abundances. Magnetite has been observed only in the oGb. Ilmenite occurs in the mGb, QD TN and btGd. It has low Al_2O_3 and MgO contents (supplementary Table S5).

Amphibole is present in almost all Solanas rocks; all the analysed crystals are calcic amphiboles (Ca_B >1.5) according to the nomenclature of Leake et al. (1997) (supplementary Table S6; Fig. 5c). The dominant amphibole in the oGb is magnesio-hornblende (Mg# = 66-80) and magnesio-hastingsite (Mg# = 70-75). Primary amphibole in the aGb and mGb is magnesio-hornblende (aGb, Mg# = 49-68; mGb, Mg# = 48-55). Amphibole in the QD, TN, aGd and btGd is mainly ferro-hornblende (Mg# = 39-42). All amphiboles have low F and Cl contents (supplementary Table S6). Secondary amphiboles, ranging in composition from actinolitic hornblende to actinolite, indicate sub-solidus alteration of the primary magmatic assemblage.

Plagioclase compositions from the studied samples span a wide range of compositions (supplementary Table S7; Fig. 6a). It forms complex zoned grains accompanied by compositional difference in anorthite content in all Solanas rocks. The cumulus grains in the oGb and aGb are An-rich, typically varying from An_{89} to An_{76}. An-poor compositions (An_{53} to An_{28}) are found in plagioclase with patchy zoning texture and in the interstitial phases. Plagioclase in the mGb ranges from bytownite (An_{84}) to andesine (An_{44}). Large plagioclase crystals with patchy zoning texture have an irregular or chequerboard, central (often) corroded core characterized by coalescence of An-rich and An-poor portions (supplementary Fig. S1). Plagioclase in QD, TN, plG and aGd, is andesine (An_{31-46}). The most evolved compositions (An_{26-39}) are found in the btGd.

Alkali feldspar from aGd and btGd varies in composition from $An_0Ab_{14}Or_{86}$ to $An_0Ab_5Or_{95}$. Alkali feldspar is rare in the QD and TN and shows a similar compositional range (Fig. 6a).

Mica occurs in almost all Solanas rocks. Micas from oGb are phlogopites (Mg# = 67-77; supplementary Table S8; Fig. 6b). Those from mGb, QD, TN, aGd and btGd are biotites (Mg# = 31-48). Among them, the biotites from mGb are the most magnesian (Mg# =45-48). F and Cl contents are low, similar to the values reported for the amphiboles (supplementary Table S8).

Apatite (41.8-44.2 wt.% P_2O_5, 53.3-55.6 wt% CaO; 0.4-3.6 wt% F; supplementary Table S9) occurs mainly as inclusions in plagioclase, amphibole and mica, suggesting early crystallisation. It is present in all rock types, but is especially abundant in the TN, aGd and btGd.

Titanite is ubiquitous and particularly abundant in the TN, aGd and btGd. Its major-element composition is homogeneous in all rock types (supplementary Table S10).

Zircon is ubiquitous as tiny grains in TN, aGd and btGd). It contains up to 4.9 wt.% HfO_2 (supplementary Table S10).

Whole-rock geochemistry

Classification and major- and trace element concentrations

The investigated Solanas rocks display a chemical composition that is very coherent with the recognized lithotype groupings (Fig. 7). The gabbroic samples fall mostly in the (subalkaline) basalt field of the TAS diagram (Fig. 7a), except for few slightly alkali-richer or silica-richer outliers from the mGb group. The mGb have significantly higher sum of alkalis (i.e. 3.23-5.07 wt.%) with respect to both aGb (1.91-3.10 wt.%) and oGb (1.13-1.70 wt.%) samples.

The TN, plG, aGd and btGd are metaluminous to weakly peraluminous (A/CNK = 0.83–1.09; A/CNK = mol. $Al_2O_3/(CaO+Na_2O+K_2O)$). The QD and TN samples fall respectively in the fields for basaltic andesite and andesite rocks, defining a quite linear increase in both silica and total alkali contents (4.25-6.21 and 4.99-6.44 wt%, respectively). This is also true for the more evolved aGd (SiO_2 = 65.2-73.6 wt%, Na_2O+K_2O = 6.25-7.81 wt%) and btGd (SiO_2 = 67.9-72.4 wt%, Na_2O+K_2O = 7.45-8.84 wt%) samples, showing a dacite/rhyolite composition. The two plG deviate quite evidently from such general trend, showing a remarkably alkali-poorer (Na_2O+K_2O = 4.32-5.84 wt%) dacite composition with respect to the aGd samples at similar SiO_2 contents (i.e. ~65 wt%). Except for the K-poorer oGb, aGb and plG, and for very few

outliers, the investigated Solanas samples depict a well-defined high-K calcalkaline series (Fig. 7b). When compared with rocks from other gabbroic complexes from the Sàrrabus area (i.e. Capo Carbonara, and Burcei) and from the northern Sardinia batholith (Punta Falcone), the Solanas rocks show a remarkably similar compositional spectrum extended to even more evolved rock types. The composition of the basic/intermediate lithotypes is also consistent with that of the basic/intermediate dykes crosscutting the entire Sàrrabus pluton.

Major elements Harker-type binary diagrams are basically in line with the previous observations, with both the oGb and aGb samples defining distinctive compositional groups (Table 1, Fig. 8). Rocks from the oGb group have the highest MgO (12.2-15.9 wt%) and CaO (11.2-13.0 wt%) and the lowest SiO_2 (46.3-49.2 wt%), Na_2O (0.77-0.96 wt%), K_2O (0.36-0.90 wt.%) and P_2O_5 (<0.08 wt%) of the entire dataset, coupled with relatively low TiO_2 and Al_2O_3 (0.31-0.37 and 13.2-15.8 wt%, respectively, comparable with values for the most evolved lithotypes). With respect to the latter, aGb rocks have lower MgO (6.24-8.35 wt%) and CaO (11.9-12.5 wt%) and higher SiO_2 (49.2-51.0 wt%), Na_2O (1.19-2.13 wt.%), K_2O (0.56-1.07 wt%) and P_2O_5 (0.07-0.15 wt%), coupled with slightly higher TiO_2 (0.45-0.54 wt.%, still unusually low for such Mg-rich compositions), low Fe_2O_3t (6.16-6.96 wt%) and the highest Al_2O_3 (19.1-21.5 wt%). All other Solanas rock samples depict quite regular differentiation trends of decreasing TiO_2 (0.24-1.74 wt%), Fe_2O_3t (1.88-12.0 wt%), MgO (0.63-6.84 wt%) and CaO (1.84-11.0 wt%) and increasing SiO_2 (47.2-73.7 wt%), and K_2O (1.30-6.66 wt%), moving from mGb to QD and TN, up to the more evolved aGd, plG (occasionally deviating, e.g. see their very low K_2O = 1.13-2.09 wt.%) and btGd rock groups, each showing relatively homogeneous

505 composition. The variation trends for Al_2O_3 and Na_2O are relatively more scattered, the
506 first defining an overall increase, while the second first increasing then decreasing. The
507 major element compositional trends of such rock samples (mGb, QD, TN, plG, aGd and
508 btGd) is basically in line with that of the rocks from the Capo Carbonara and Punta
509 Falcone complexes. The rocks from the Burcei complex also fall within such
510 compositional field, though showing a more restricted range of intermediate-evolved
511 lithotypes (e.g. SiO_2 = 57.3-66.7 wt%, MgO = 1.23-4.59 wt%, CaO = 3.24-7.55 wt%,
512 K_2O = 1.98-4.24 wt%), basically consistent with that covered by the Solanas TN, plG and
513 aGd. The composition of the basic/intermediate dykes intruding the Sàrrabus pluton is on
514 the whole comparable to that of the Solanas mGb (except for slightly higher MgO, up to
515 7.86-9.90 wt%), although some data scattering is also evident (likely ascribable to their
516 weak preservation status, i.e. LOI frequently >3 wt% and up to 4.75-6.24 wt%).
517 Trace elements variation trends are definitely much more scattered, although, on the
518 whole, in line with those defined by major elements (Table 2, Fig. 9). Samples from the
519 oGb group are distinctively separated from all the others due to their much higher Ni (22-
520 47 ppm) and Cr (465-820 ppm), and their low V (106-138 ppm), Y (4-14 ppm), Nb (<3
521 ppm) and Zr (29-54 ppm), comparable with, or even lower than, those for the more
522 evolved Solanas rocks. Rocks from the aGb group also have relatively high Cr (75-240
523 ppm) and unusually low Y (4-17 ppm), Nb (bdl) and Zr (46-83 ppm), coupled with the
524 highest Sr concentrations observed for the entire dataset (462-548 ppm). As for the
525 remaining lithotypes, the following general variation trends can be envisaged: 1)
526 decreasing Sr (from 290-373 to 112-247 ppm), Ni (6-14 to <9 ppm), Cr (21-76 to <29
527 ppm), Sc (38-51 to <21 ppm), V (193-286 to 33-121 ppm) and Y (32-66 to 8-41 ppm); 2)

increasing Rb (33-75 to 85-158 ppm); 3) Ba firstly increasing (from 412 to 1117 ppm at MgO ~3 wt%), then decreasing down to 528 ppm. Some major deviations are represented by three extremely Ba-rich aGd and btGd samples (Ba = 1614-1891 ppm), three QD and plG sample L55 with Sr up to 364-379 ppm, and one plG sample with Rb down to 34 ppm. Trace elements data for the rocks from Capo Carbonara, Punta Falcone and Burcei are on the whole again in line with those of the Solanas rocks, except for the oGb and aGb rock groups. The most evident differences are represented by the higher Ni (52-170 ppm) and Cr (342-823 ppm) contents of some Capo Carbonara samples and by the higher V (325-836 ppm) and lower Zr (58-117 ppm) of some Punta Falcone rocks. The Sàrrabus dykes are again very similar to the Solanas mGb although include lithotypes with significantly higher Ni and Cr (respectively 66-200 and 144-518 ppm) and slightly lower Nb and Zr.

Chondrite- and primitive mantle-normalized multi-element diagrams

Normalized multi-element "spider-diagrams" for the investigated Solanas rocks are reported in Figs. 10 and 11. Among gabbro samples, oGb and aGb are the least enriched (chondrite-normalized abundances below 25 and 50, respectively), with slight Light to Heavy Rare Earth Elements enrichment (LREE/HREE, e.g. La_N/Yb_N = 4.38 and 5.89, respectively), small Eu trough [$Eu/Eu^* = Eu/(Sm*Gd)^{1/2}$ = 0.88 and 0.96, respectively] and relatively flat patterns in the MREE and HREE region (e.g. Dy_N/Lu_N = 1.27 and 1.19, respectively; Fig. 10a). The mGb rocks display very similar subparallel patterns which are more enriched (~125 times chondritic values) and have a much more evident Eu

551 trough (Eu/Eu* = 0.62-0.68) with respect to oGb and aGb rocks. In primitive mantle-
552 normalized plots (Fig. 11a) all the gabbro samples have subparallel patterns with marked
553 peaks at Large Ion Lithophile Elements (LILE; e.g. Cs, Rb, Ba) and Pb, and troughs at
554 High Field Strength Elements (HFSE; Nb, Ta and Ti), similar to those for typical
555 subduction-related magmas and for the average subducting sediments (i.e. the GLObal
556 Subducting Sediments GLOSS-2 estimate). The oGb and aGb rocks have the lowest
557 normalized abundances and display also some evident peak at Sr, not featured by mGb
558 samples. The chondrite-normalized multi-element patterns displayed by the gabbroic
559 samples from Capo Carbonara and Punta Falcone basically cover the same compositional
560 spectrum defined by the Solanas gabbro samples and display the same peculiar GLOSS-
561 2-like fingerprint (Figs. 10d,e, and 11d,e). The same can be said for the Sàrrabus dykes,
562 which include also some more enriched intermediate compositions (e.g. with LREE up to
563 ~300-800 times chondritic abundances; Figs. 10f and 11f).

564 Intermediate samples of the QD and TN groups include both rocks with very peculiar
565 chondrite- (Ch) and primitive mantle-normalized (PM) patterns as well as rocks strongly
566 resembling mGb samples (Figs. 10b and 11b). The latter have only slightly higher (or
567 even lower) normalized abundances for the most incompatible elements with respect to
568 the less evolved mGb, as well as slightly higher LREE/HREE (La_N/Yb_N = 7.51-15.8),
569 similar or slightly smaller Eu troughs (Eu/Eu* = 0.61-0.87), and comparable LILE/HFSE
570 enrichment and MREE-HREE flat patterns, with respect to the former. Extremely similar
571 patterns are also observed for the rocks from the Burcei complex (Figs. 10f and 11f). On
572 the other hand, QD sample L57 and TN sample L15 have generally lower normalized
573 abundances (i.e. below 100 times chondritic values for the most incompatible elements),

574 coupled with evident Eu peaks (Eu/Eu* = 1.86-1.88) and low MREE/HREE (e.g.
575 Dy_N/Lu_N = 0.79-1.05).

576 The strongly evolved Solanas rocks also display quite variable normalized patterns
577 (Figs. 10c and 11c). The patterns for L13 aGd and L27 btGd samples are similar to those
578 for mGb rocks, with slightly higher incompatible element abundances and deeper Eu
579 troughs (Eu/Eu* = 0.54-0.66). The L55 plG sample is quite similar to the above
580 "anomalous" QD and TN samples, with very low normalized abundances (<60 x Ch), a
581 strong Eu peak (Eu/Eu* = 3.80) and a marked MREE/HREE depletion (Dy_N/Lu_N = 0.64).
582 Similar patterns can be observed also for L16 plG and L81 aGd samples, though with
583 smaller Eu peaks (Eu/Eu* = 1.30 and 1.40, respectively) and less pronounced
584 MREE/HREE depletion (Dy_N/Lu_N = 1.00 and 0.92, respectively).

585

586 ## Sr-Nd isotope systematics

587 Most of the investigated rock samples from the Solanas complex have a quite
588 homogenous composition in terms of initial Sr and Nd isotope ratios. The Rb-Sr three-
589 point (biotite, amphibole and whole-rock) isochron on a QD sample (GLR16) yielded an
590 age of 299.6 ± 0.3 Ma (mean square of weighted deviates; MSWD = 3.2; Franciosi 1999;
591 supplementary Fig. S2). This age is similar (within error) to Rb-Sr ages reported by
592 Brotzu et al. (1983) for Burcei (311 ± 9 Ma) and Nicoletti et al. (1982) for Capo
593 Carbonara plutons (301 ± 3 Ma). In absence of high-precision age determinations for
594 Solanas igneous rocks, we corrected Nd-Sr isotopes to an age of 300 Ma (Table 2, Fig.
595 12). The $(^{87}Sr/^{86}Sr)_i$ values are remarkably radiogenic, spanning the 0.70882-0.70933
596 range for mGb, 0.70886-0.70976 for QD, 0.70892-0.70905 for TN, 0.70927-0.70944 for

plG, 0.70827-0.70932 for aGd and btGd. These are coupled with unradiogenic $(^{143}Nd/^{144}Nd)_i$ values of 0.51194 for mGb, 0.51190-0.51195 for QD, 0.51196-0.51199 for TN, 0.51194-0.51196 for plG, 0.51194-0.51198 for aGd and btGd. Both oGb and aGb samples display a remarkably distinct isotopic signature, with the first having a significantly lower $(^{87}Sr/^{86}Sr)_i$ of 0.70672, the second a slightly higher $(^{143}Nd/^{144}Nd)_i$ of 0.51202, with respect to most of the samples.

All the Solanas rocks fall well within the compositional field defined by the literature samples for the Sardinia-Corsica batholith, which extends also to lower and higher values of initial Sr-isotope ratio, and the reverse is for Nd-isotope ratio [i.e. $(^{87}Sr/^{86}Sr)_i$ = 0.70460-0.71113, $(^{143}Nd/^{144}Nd)_i$ = 0.51185-0.51230]. An exception to this is represented by few anomalous samples from Conte et al. (2017) lying in or close to the Sr- and Nd-depleted quadrant (Fig. 12). The Sàrrabus dykes also fall well within this field, displaying quite large ranges for both $(^{87}Sr/^{86}Sr)_i$ and $(^{143}Nd/^{144}Nd)_i$ values (0.70515-0.70968 and 0.51197-0.51222, respectively).

Estimates of the emplacement conditions of the Solanas magmas

Estimates of emplacement/storage depths of the Solanas magmas were made using both mineral (i.e. amphibole-plagioclase pair) and bulk-rock (i.e. apatite and zircon saturation) compositions. However, it should be noted that these data are strongly dependent on the calibration of the thermobarometers employed and, therefore, can provide only provisional geological information.

Apatite and zircon thermometry (Watson and Harrison 1983; Harrison and Watson 1984) were applied to the Solanas rocks that show evidence of saturation in P_2O_5 and Zr (TN, aGd and btGd). P_2O_5 and Zr decrease with increasing SiO_2 (Figs. 8 and 9), implying crystallisation of apatite and zircon, hence, saturation of the parent melts in the two elements. The apatite thermometer gives temperatures in the following ranges: 854-910 °C (TN), 888-941 °C (aGd) and 854-955 °C (btGd). The zircon thermometer gives lower temperature estimates of 753-812 °C (TN), 787-812 °C (aGd) and 767-787 °C (btGd), respectively. The difference between apatite and zircon saturation temperatures has been attributed to several possible causes, such as: 1) excess apatite, which may not fractionate efficiently from the melt; 2) the saturation model may not be appropriate for the rocks considered (e.g. Hoskin et al. 2000); 3) lower temperature estimates of zircon thermometer representing temperatures closer to the solidus (e.g. Anderson 1996). Equilibration temperatures for hornblende-plagioclase assemblages were calculated iteratively following the method of Anderson and Smith (1995). The calculated temperatures (edenite-richterite thermometers) for the TN, aGd and btGd are of 759-778 °C, 720-755 °C and 730-760 °C, respectively, on the whole similar to those obtained using the zircon thermometer.

Pressure estimates for TN, aGd and btGd amphiboles were calculated using the temperature-corrected Anderson and Smith (1995) geobarometer. Application of this technique requires the presence of the appropriate buffering assemblage of hornblende, plagioclase, K-feldspar, biotite, quartz, Fe-Ti oxide (magnetite or ilmenite), apatite and titanite. Because the uncertainty in pressure determinations using the Anderson and Smith (1995) method is ± 0.6 kbar, the corresponding uncertainty in emplacement depth would

642 be ± 2.1 km. Calculated pressures for TN range between 2.7 and 3.3 kbar, which
643 correspond to crystallisation depths between 8.9 and 10.9 km, respectively. The pressures
644 obtained for the aGd and btGd range from 2.6 to 4.0 kbar (8.6-13.2 km).

645 Thermobarometric estimates for mGb were obtained using the formulations of Ridolfi
646 et al. (2010). This method uses an entirely empirical approach, linking thermobarometric
647 equations exclusively to volcanic and experimental amphibole composition. Application
648 of this method requires that amphiboles crystallised from calc-alkaline magmas have Al#
649 $\leq$0.21 [Al# = $^{VI}Al/(^{VI}Al+^{IV}Al)$] and $Mg/(Mg+Fe^{2+})$ >0.5. Calculated pressures range from
650 1.4 to 1.8 kbar, corresponding to depths of 4.6-5.9 km. Temperature estimates range from
651 768 to 836 °C.

652 Water content in the silicic magmas (TN, aGd and btGd) can be estimated empirically
653 by comparison with available experimental data. Scaillet et al. (1998) indicated that most
654 silicic volcanic rocks and their plutonic equivalents have a dissolved H_2O content of 4-6
655 wt% for a wide temperature range (650-900°C). Scaillet and Evans (1999) and
656 Dall'Agnol et al. (1999) proposed experimental calibrations of water contents in magmas
657 of dacitic and rhyolitic composition, at 2.2 and 3.0 kbar. The pressure and temperature
658 conditions for the emplacement of the Solanas silicic rocks, which are not far from these
659 experimental data, allow the water fugacity to be roughly estimated for the parent melt of
660 the felsic rocks. Accordingly, the phase relationships in these rocks (stability of
661 hornblende, and plagioclase with anorthite content less than An_{50}) suggest water contents
662 $\geq$ 6 wt%. On the basis of the experimental data of Scaillet and Evans (1999) and using
663 representative Al_{tot} values of hornblende (1.3-1.5 apfu), the water content in the 750-
664 850°C temperature range is estimated to be around 5.5-6.5 wt%.

Discussion

The present study on the Solanas igneous rocks has revealed the presence of a large variety of lithotypes, spanning the entire compositional spectrum from Mg-rich to strongly evolved Mg-poor terms. This feature is even more peculiar considering the relatively narrow areal extension of the complex (~0.4 km^2; Fig. 1c). Although the limited areal extension and the relatively coherent petrochemical features displayed by all the observed lithotypes would suggest a genetic model implying a common origin for all the Solanas magmas, several lines of evidence can be raised against this. These include: 1) complex field relationships between the outcropping bodies (e.g. microgabbroic blob-like enclaves hosted by tonalitic-quartz dioritic masses); 2) large ranges of mineral composition within the same lithotype (e.g. plagioclase crystals from the gabbroic rocks), commonly associated with complex zoning patterns; 3) the presence of three different types of gabbroic lithotypes with distinctive petrochemical features; 4) some major scattering of trace element abundances; 5) variable, strongly Sr-radiogenic and Nd-unradiogenic compositions, suggestive for the involvement of crustal components in the genesis of the emplaced magmas.

On such basis, it appears evident that reconstructing the petrogenetic history of the Solanas rocks is particularly challenging, as many magma-genetic and evolutionary processes might have acted concurrently, as it is common in post-collisional geodynamic settings (e.g. Wang et al. 2004; Prelević and Seghedi 2013; Wang et al. 2014; Couzinié et al. 2016; Fedele et al. 2016). As a consequence, the effects of such processes could have overlapped, making their correct recognition (and appropriate quantitative treatment)

688 extremely difficult. Possible petrogenetic processes for the origin of the Solanas mafic
689 and silicic rocks can be variable differentiation of mantle-derived magmas by fractional
690 crystallization, partial melting of underplated igneous rocks, or partial melting of
691 continental crust. Mixing and mingling can also to be considered as possible processes
692 for the genesis of the Solanas rocks. The following sections are thus aimed at addressing
693 all the various processes related with the genesis of the recognized lithotypes cropping
694 out in the Solanas area, in an effort to shed some additional light on the petrogenesis of
695 the numerous complexes making up the Sardinia-Corsica batholith. We will deal first
696 with the less evolved, gabbroic rocks, in order to unravel their mutual relationships and
697 their possible linkage with sources in the mantle, then with the possible recognition of
698 any sort of genetic lineage(s) among the various magma types. Alternative magma-
699 genetic processes will be then taken into account for those lithotypes that do not seem to
700 be genetically related with the others.
701

702 ## Mafic-silicic magma interactions

703 Several igneous rocks of the Solanas complex can be considered as hybridized, as shown
704 by field and textural evidences: mafic enclaves, widespread occurrence of plagioclase
705 xenocrysts and, in minor amounts, of biotite and hornblende (in particular in the mGb)
706 and plagioclases with patchy zoned texture and corroded rims (Fig. 2b,c,d).
707 In any magma interaction, the relative volumes of the two interacting materials play an
708 important role. If there is a large influx of mafic magma there may be an insufficient
709 quantity of cooler silicic host magma to chill against, and therefore mixing is preferred.
710 Alternatively, when very small amounts of mafic magma are injected into large quantities

of silicic magma, mingling more readily occurs and mafic enclave formation may be favored. In the case of the mingling structures observed in the Solanas complex, the presence of blocks of mafic material within larger volumes of silicic host suggests that smaller volumes of mafic magma were injected, promoting mafic enclave formation.

The gabbroic rocks of the Solanas complex and their relationship with mantle sources

The oGb and aGb have whole-rock major and trace element compositions reflecting their cumulus origin. The oGb are particularly enriched in MgO (up to 16 wt. %) and Cr (465-820 ppm), while the aGb are high in CaO (>12 wt.%) and Al_2O_3 (>21 wt.%; Table 1). In addition, the compositional range of plagioclase (An_{76-89}), olivine (Fo_{68-76}) and clinopyroxene (Mg# = 78-86) in the oGb (Supplementary Tables S1, S2 and S6) are typical of arc cumulates (Fig. 13). Factors commonly argued to be responsible for crystallisation of such calcic-plagioclase include high magmatic water contents (Arculus and Wills 1980; Sisson and Grove 1993; Panjasawatwong et al. 1997), high Ca/(Ca+Na) in the melt and low crystallisation pressures (Panjasawatwong et al. 1997).

The olivine, orthopyroxene and clinopyroxene crystals occasionally enclosed in the amphibole from the oGb can be interpreted as remnants of dismembered mafic material that has reacted with the amphibole-forming melt. The origin of these mineral phases could be attributed to their early crystallisation from a basaltic melt that subsequently stabilized amphibole. Convective melt movements in a chemically-stratified magma chamber may have allowed the sampling of these cumulitic phases by a water-rich

733 magma. Compositional differences between the amphiboles of the oGb and the aGb
734 indicate that these rocks crystallised from magmas that had different bulk chemistry.
735 To determine the Mg# of the possible parental melt of oGb, we used mineral-melt
736 equilibrium equations with $K_d^{Fe–Mg}$ values of 0.30 for olivine (Roeder and Emslie 1970),
737 0.27 for clinopyroxene (Putirka, 2008) and 0.42 for amphibole (Nandedkar et al. 2016).
738 The calculated Mg# of the melts in equilibrium with olivine cores varies between 0.40
739 and 0.47. Magnesium numbers ranging from 0.49 to 0.56 were calculated for the melts in
740 equilibrium with clinopyroxene cores, whereas Mg# of the magmas in equilibrium with
741 intercumulus amphibole varies from 0.50 to 0.64. This suggests that olivine,
742 clinopyroxene and amphiboles derived from different magmas.
743 The mGb have MgO (<7 wt.%) and Al_2O_3 (>16 wt.%) typical of high-Al basalts
744 (Kersting and Arculus 1994). These rocks represent relatively evolved magma in terms of
745 Mg# (52-58). Primitive mantle-normalized diagrams (Fig. 11a) show patterns typical of
746 magmas emplaced in collisional tectonic settings and/or magmas that experienced upper
747 crustal contamination at shallow depths, such as: i) troughs at Nb-Ta and ii) peaks for Pb
748 (with values as high as 150-250 times primitive mantle). As regards mantle sources, a
749 detailed characterization is hampered due to the recalled relatively differentiated (low
750 Mg#, Ni and Cr) and hybridized nature of mGb rocks (presence of plagioclase,
751 hornblende and biotite xenocrysts captured from the host magma during the interaction
752 between the basic and acid magma). However, on the basis of the flat HREE pattern in
753 chondrite-normalized diagrams, we argue a N-MORB-like spinel-bearing lherzolite,
754 variably metasomatized by fluids from subducted oceanic crust, as a possible mantle
755 source. Ratios among trace elements variably compatible with fluid and melt phases (i.e.

Th/Pb = 0.09-0.36, Th/Nd = 0.04-0.11 and Sr/Nd = 6.20-8.48) exclude the contribution of melts from subducted slab.

The Sr and Nd isotope systematics indicates that the Solanas magmas are consistent with derivation from a subduction-metasomatized mantle source and crustal contamination processes (Fig. 12). When considered in the framework of the other rocks from the Sàrrabus pluton as well as the late dikes, the initial Sr-Nd isotopic compositions of the Solanas rocks may represent part of a binary mixing trend. The two end-members might be an enriched mantle source and an upper continental crust component.

In the geodynamic context of the Sardinia-Corsica batholith, formed after the collision between Gondwana and Armorican plates, the local mantle sources might have been affected by geochemical and isotopic modifications related with subduction process(es) predating the plates collision (Carmignani et al. 1994). The significant contribution by an upper continental crust component might have been involved in at least two ways. One possible scenario is that of mafic magmas derived by the subduction-modified local mantle sources, subsequently evolving through open-system AFC-type processes, assimilating crustal rocks in variable amounts. Another possibility is that the thermal anomaly that likely affected the local crust during and after the collision phases induced crustal anatexis generating felsic melts that mixed in variable proportions with mantle-derived melts (e.g. Conte et al. 2017)

Magmatic lineages and differentiation processes in the Solanas complex

The Solanas samples form good linear trends vs. MgO for many major and trace elements (Fig. 8 and 9). Such linear trends may be caused by fractional crystallisation

779 processes. Two fractional crystallization scenarios were hypothesized: 1) the origin of
780 aGd and btGd (L81, a leucocratic border-facies of aGd) by fractional crystallisation of a
781 quartz-dioritic parental magma (L14), and 2) the origin of plG by fractional
782 crystallisation from QD (L57). Least-squares mass balance calculations (Stormer and
783 Nicholls 1978; supplementary Table S11) indicate that 58% fractional crystallisation of a
784 gabbroic assemblage (65% plagioclase 19% biotite, 16% ferro-hornblende, 1% apatite) is
785 required in the transition from QD (L14) to TN (L33). In the transition TN (L33) to aGd
786 (L13), the removed cumulate (20%) is formed by plagioclase (46%), ferro-hornblende
787 (40%), biotite (12%) and apatite (2%). The transition from aGd (L13) to btGd (L81) is
788 modeled by 39% fractional crystallisation of plagioclase (55%), ferro-hornblende (27%),
789 biotite (17%) and apatite (1%). Mass balance calculations (supplementary Table S11)
790 predicted that the plG (L16,55) could be produced from a quartz-dioritic magma (L57) by
791 removal of 58% of an assemblage consisting of 57% plagioclase, 26% biotite, 16% ferro-
792 hornblende and 1% apatite. A good agreement between model and analytical data is
793 observed also for REEs (supplementary Fig. S3). The addition of 0.003-0.01% zircon to
794 the cumulate is needed to account for HREE, Zr, Y and Hf behaviour.

795 The geochemical variability between samples of the QD-TN-plG-aGd-btGd
796 association indicates that the Solanas igneous complex is compositionally diverse
797 (especially evident for elements such as Zr, Y and REEs), despite the limited Sr-Nd
798 isotopic variation. This precludes any genetic link between these types of silicic rocks
799 and, therefore, suggests that they originated from distinct magmas.

800 Partial melting of mafic lower crust or underplated basaltic rocks is also a plausible
801 hypothesis for the genesis of Solanas silicic magmas. However, experimental works show

802 that water-saturated melting of basaltic rocks, amphibolites and greenstones at 1, 3, 6.9
803 and 10 kbar pressure (Helz, 1976; Spulber and Rutherford, 1983; Beard and Lofgren,
804 1991; Wolf and Wyllie, 1994) should produce liquids with higher Al_2O_3 and CaO
805 contents than the Solanas QD and TN (supplementary Fig. S4). The plG, aGd and btGd
806 may have been produced by partial melting of mafic lower crust or underplated basaltic
807 rocks.

808 The absence of primary minerals such as muscovite, cordierite, garnet,
809 aluminosilicates (andalusite or sillimanite) and tourmaline in the Solanas rocks also
810 excludes an origin for these rocks as anatectic melts of metasedimentary protoliths.

811 Initial Sr-Nd isotopic ratios ($^{87}Sr/^{86}Sr_i$ = 0.70672-0.70976; $^{143}Nd/^{144}Nd_i$ = 0.511900-
812 0.512020) are outside the range of typical mantle compositions. Therefore, hybridization
813 between mantle- and crustal-derived magmas or assimilation and fractional
814 crystallization (AFC) is a reasonable hypothesis for the genesis of the Solanas rocks.

815 The T_{DM} Nd model ages (one stage) for the Solanas rocks range from 1.0 to 1.5 Ga
816 (Table 2). These values are generally lower of the granitoids of southern Sardinia (1.4-2.3
817 Ga; Conte el al. 2017) and suggest that the crustal contaminant contain Nd with an
818 average Proterozoic crustal residence time.

819

820 On the unusual petrochemical composition of some Solanas rocks

821 As resulting from the previous sections, in order to explain the genesis of the Solanas
822 rocks a rather complex model, accounting for the observed variability in terms of both
823 petrology and geochemistry, seems to be required. In this framework, some samples have
824 displayed a distinctive peculiar petrochemical composition that further argues for some

additional petrogenetic variability. This is particularly evident for the plG samples (especially L55), but also extends to some QD (L57), TN (L15) and btGd (L81) samples, all being characterized by Eu peaks and low MREE/HREE in the chondrite- and mantle-normalized multi-element plots (see section 4.3.2). On such basis, it could be tentatively proposed that these samples should be considered as part of an independent magmatic lineage similar to the tonalite-trondhjemite-granodiorite (TTG) suites that were extremely common during the Archean (e.g. Martin et al. 2005). These magmas are generally considered the ancient analogue of modern adakites, therefore representing the product of melting of a mafic source rock (possibly including also some interaction with mantle peridotite; e.g. Defant and Drummond 1990; Martin et al. 2005, 2014; Moyen 2009; Castillo 2012; Palin et al. 2016).

The Solanas plG, QD, TN and btGd with anomalous composition reported above have very few compositional similarities with typical TTG/adakitic magmas (Martin et al. 2005). Namely: 1) QD and TN are relatively poor in SiO_2 (56.1-59.9 wt.%, where TTGs have SiO_2 >64 wt.%); 2) Na_2O is at the lower end of the typical TTG compositional range (i.e. 3.15-3.75 wt.% vs. $3.0 \leq Na_2O \leq 7.0$ wt.%), and even below the lower limit for L81 btGd sample (2.47 wt.%); 3) K_2O/Na_2O is high (0.65-2.17 vs. <0.5 of TTGs) except for the plG samples (0.36-0.56); 4) the sum of ferromagnesian elements is very high (Fe_2O_3tot+MgO+MnO+TiO_2 = 7.89-12.3 wt.% vs. <5.0 wt.%), except for L81 btGd (2.79 wt.%); 5) La_N/Yb_N is only moderately high (8.92-17.4 up to 32.1 in L81 btGd) compared to the most extreme values up to 150 recorded for some TTG rocks; 6) in the discriminative plots of Fig. 14, only few of this Solanas samples plot well within the typical field for TTG/adakitic rocks. In this light, it seems unlikely that the origin of such

unusual Solanas samples has to be ascribed to that responsible for the genesis of the typical TTG/adakite magmas. This is also supported by both the paucity and the random outcropping location of such samples, which thus suggests that other processes, likely acting at a very local scale, rather than larger-scale melting of a mafic source (or a high-Sr/Y crustal source at P~5-10 kbar; Moyen 2009), were responsible for their peculiar TTG/adakite-like geochemical signature.

Proposed alternative ways to obtain the typical high Sr/Y and La/Yb characterising TTG/adakitic rocks involve i) significant fractionation of Sr-rich and Y-poor amphibole (±apatite) crystals at shallow depths or ii) deep-level fractionation of mineral assemblages mainly consisting of garnet and high-pressure Mg-rich amphibole (e.g. Castillo 2012; Ribeiro et al. 2016). The latter seems not suitable for the Solanas rocks considered here, as this would result in remarkably high HREE/LREE and HREE/MREE, given the renown preferential partitioning of HREEs within garnet lattice (i.e. $^{garnet/melt}D_{HREE}$ >60; e.g. Taylor et al. 2015). On the other hand, amphibole fractionation seems a more viable process, as this would easily explain the observed depletion in MREE, more preferentially partitioned in amphibole crystals with respect to both LREE and HREE (e.g. Nandedkar et al. 2016). Whether amphibole is a quite common phase in the Solanas QD and TN, it should be observed that this phase is rare in the plG and btGd rocks. In these two, the characteristic depletion in MREE could have been achieved through fractionation of apatite and titanite, both commonly found as accessory phases and both preferentially hosting MREEs with respect to LREE and HREE (e.g. Prowatke and Klemme 2005, 2006a,b). In addition, some evidence for accessory zircon fractionation can be retrieved from the contents of trace elements like HREE and Y,

871 which are known to be concentrated in this phase. We note indeed that the composition of
872 btGd L81 shows relative depletion of HREE and Y and roughly half Hf concentration
873 when compared to TN L33 (Hf = 6.9 vs. 3.2 ppm). We take this feature as our best
874 evidence for zircon removal.
875

876 ## Geodynamic implications

877 Ages similar to those of the Solanas rocks (~300 Ma) are found in other plutonic
878 complexes of Sàrrabus (Brotzu et al. 1983; Nicoletti et al. 1982) suggesting that the
879 Solanas intrusion represents part of a regional magmatic episode. Following major crustal
880 thickening and subsequent post-collisional collapse during the Late Carboniferous-Early
881 Permian (315–285 Ma: Cocherie et al. 2005), the Sardinia basement underwent an
882 episode of extension, with a widespread magmatic activity (forming the Sardinian portion
883 of the Sardinia-Corsica batholith) including intrusion of mafic magmas, and development
884 of small continental basins (filled by calc-alkaline volcanics and sedimentary rocks).
885 Partial melting involved different source components (1) middle-lower crust levels
886 formed during the Ordovician crustal accretion event through underplating of mantle-
887 derived magmas (e.g. Tommasini et al., 1999); (2) upper-crustal levels mainly composed
888 by sedimentary and silicic igneous rocks (e.g. Di Vincenzo et al., 1996); (3)
889 subcontinental mantle enriched by recycling of crustal material (Tommasini et al. 1995).
890 In the Sàrrabus area, lines of evidence in favor of mantle involvement are the close field
891 association between the gabbro-tonalitic complexes (Solanas, Burcei, Torre de su
892 Fenugu, Villasimìus, Capo Carbonara) and the mafic dike swarms.

The dispersion of Sr and Nd isotope data for Variscan magmatic rocks in the Sardinia-Corsica batholith highlights the wide diversity of materials involved in their genesis (Fig. 12). However, if the dioritic-tonalitic-granodioritic magmas of Solanas were in fact derived from fractional crystallization of mafic parental magmas, this would suggest that subcontinental mantle was an active and important component contributing to magmatism in different parts of Sàrrabus pluton and should be taken into account in geochemical models of Variscan magmatic evolution.

Conclusions

An integrated study involving mineral chemistry, whole-rock and Sr-Nd isotope geochemistry combined with detailed field investigation was carried out for the composite Solanas calc-alkaline intrusion (Sàrrabus pluton) to probe the origin of its compositional diversity. The Solanas intrusion is composed of olivine gabbronorites, amphibole gabbros, microgabbros, quartz-diorites, tonalites, plagiogranites, amphibole-granodiorites and biotite-granodiorites (plus deeply altered quartz gabbros, not investigated here). Mineral phases and their compositions were used to estimate the physicochemical parameters of their crystallising parent magmas. The intermediate and evolved rocks crystallised under conditions of 2.7-4.0 kbar pressure and 720-778 °C temperature.

The various bodies of the intrusion exhibit distinct geochemical fingerprints, indicating that the Solanas complex was constructed from different magma pulses, rather than by crystallisation of a single large batch of magma. The favoured hypothesis for the petrogenesis of the Solanas intermediate and evolved rocks is a prolonged differentiation

starting from different quartz-dioritic parental magmas, accompanied by variable crustal contamination prior to the final emplacement.

The olivine gabbronorites and amphibole gabbros have textural and geochemical features of cumulates from two distinct hydrous basaltic magmas.

The multi-element patterns of mGb with spikes in Cs, Ba and Pb, and troughs in Nb and Ta, are consistent with magma sources involving melting of a HFSE-depleted mantle that has been fluxed by fluids following dehydration of a subducted slab.

Plutonic rocks derived from mafic magmas, together with wide mafic dike swarms in the Sàrrabus region, point out a significant role of the subcontinental mantle in southern part of the Variscan batholith.

Acknowledgements

Leone Melluso and Vincenzo Morra are gratefully acknowledged for stimulating discussions. Sergio Bravi provided generous support with thin sections preparation. This study has been granted by Fondi Ricerca di Ateneo (DR_3450_2016 to C. Cucciniello) and PRIN 2015 (20158A9CBM to Leone Melluso). We sincerely thank Prof. Pietro Brotzu, who provided invaluable experience and scientific input.

References

Anderson JL, (1996) Status of thermobarometry in granitic batholiths. Transactions of the Royal Society of Edinburgh 87:125-138

Anderson JL, Smith DR (1995) The effects of temperature and fO_2 on the Al-in-hornblende barometer. Am Mineral 80:549-559

939 Arculus RJ, Wills KJA (1980) The petrology of plutonic blocks and inclusions from the
940 Lesser Antilles island arc. J Petrol 21:743–799
941 Barbey P, Gasquet D, Pin C, Bourgeix AL (2008) Igneous banding, schlieren and mafic
942 enclaves in calc-alkaline granites: The Budduso pluton (Sardinia). Lithos 104:147-163
943 Beard JS (1986) Characteristic mineralogy of arc-related cumulate gabbros: implications
944 for the tectonic setting of gabbroic plutons and for andesite genesis. Geology 14:848-
945 851
946 Beard JS, Lofgren GE (1991) Dehydration melting and water-saturated melting of
947 basaltic and andesitic greenstones and amphibolites at 1, 3 and 6.9 kb. J Petrol
948 32:365–401
949 Bralia A, Ghezzo C, Guasparri G, Sabatini G (1982) Aspetti genetici del batolite sardo-
950 corso. Rend Soc It Mineral Petrol 238:701–764
951 Brotzu P, Morbidelli L, Traversa G (1978) Caratteri petrografici e chimici delle sieniti
952 del Sarrabus meridionale (Sardegna sud-orientale). Per Mineral 47:83-98
953 Brotzu P, Callegari E, Secchi A (1993) The search for the parental magma of the high-K
954 calcalkaline igneous rock series in the southernmost Sardinia Batholith. Per Mineral
955 62:253-280
956 Burns LE (1985) The Border Ranges ultramafic and mafic complex, south–central
957 Alaska: cumulate fractionates of island–arc volcanics. Can J Earth Sci 22:1020–1038
958 Cappelli B, Carmignani L, Castorina F, Di Pisa A, Oggiano G, Petrini R (1992) A
959 Hercynian suture zone in Sardinia: geological and geochemical evidence. Geodin Acta
960 5:101–118

961 Carmignani L, Carosi R, Di Pisa A, Gattiglio M, Musumeci G, Oggiano G, Pertusati PC
962 (1994) The Hercynian chain in Sardinia (Italy). Geodin Acta 7:31–47
963 Carmignani L, Oggiano G, Funedda A, Conti P, Pasci S (2015) The geological map of
964 Sardinia (Italy) at 1:250,000 scale. J Maps doi: 10.1080/17445647.2015.1084544
965 Casini L, Cuccuru S, Maino M, Oggiano G, Tiepolo M (2012) Emplacement of the
966 Arzachena Pluton (Corsica–Sardinia Batholith) and the geodynamics of incoming
967 Pangaea. Tectonophysics 544–545:31–49
968 Casini L, Cuccuru S, Puccini A, Oggiano G, Rossi Ph (2015) Evolution of the Corsica-
969 Sardinia batholith and late-orogenic shearing of the Variscides. Tectonophysics
970 646:65–78
971 Cocherie A, Rossi P, Fouillac AM, Vidal P (1994) Crust and mantle contributions to
972 granite genesis—an example from the Variscan batholith of Corsica, France, studied
973 by trace element and Nd–Sr–O-isotope systematics. Chem Geol 115:173–211
974 Cocherie A, Rossi Ph, Fanning CM, Guerrot C (2005) Comparative use of TIMS and
975 SHRIMP for U-Pb zircon dating of A-type granites and mafic tholeiitic layered
976 complexes and dykes from the Corsican Batholith (France). Lithos 82:185–219
977 Conte AM, Cuccuru S, D'Antonio M, Naitza S, Oggiano G, Secchi F, Casini L, Cifelli F
978 (2017) The post-collisional late Variscan ferroan granites of southern Sardinia (Italy):
979 inferences for inhomogeneity of lower crust. Lithos 294–295:263–282
980 Couzinié S, Laurent O, Moyen J-F, Zeh A, Bouilhol P, Villaros A (2016) Post-collisional
981 magmatism: crustal growth not identified by zircon Hf-O isotopes. Earth Planet Sci
982 Lett 456:182-195

983 Cruciani G, Montomoli C, Carosi R, Franceschelli M, Puxeddu M (2015) Continental
984 collision from two perspectives: a review of Variscan metamorphism and deformation
985 in northern Sardinia. Per Mineral 84:657–699
986 Cuccuru S, Naitza S, Secchi F, Puccini A, Casini L, Pavanetto P, Linnemann U,
987 Hofmann M, Oggiano G (2016) Structural and metallogenic map of late Variscan
988 Arbus Pluton (SW Sardinia, Italy). J Maps 12:860–865
989 Dack AV (2009) Internal Structure and Geochronology of the Gerrei Unit in the
990 Flumendosa Area, Variscan External Nappe Zone, Sardinia, Italy. M. A. Thesis.,
991 Boise State University. Idaho, USA.
992 Dall'Agnol R, Scaillet B, Pichavant M (1999) An experimental study of a lower
993 Proterozoic A-type granite from the Eastern Amazonian Craton, Brazil. J Petrol
994 40:1673-1698
995 Deer WA, Howie RA, Zussman J (1992). An Introduction to the Rock-forming Minerals.
996 Harlow: Longman, pp 696
997 Defant MJ, Drummond MS (1990) Derivation of some modern arc magmas by melting of
998 young subducted lithosphere. Nature 347:662–665
999 Del Moro A, Di Simplicio P, Guezzo C, Guasparri G, Rita F, Sabatini G (1975).
1000 Radiometric data and intrusive sequence in the Sardinia batholith. Neues Jahrb
1001 Mineral Abh 126:28-44
1002 De Paolo DJ (1981) Trace element and isotopic effects of combined wall rock
1003 assimilation and fractional crystallization. Earth Planet Sci Lett 53:189–202
1004 De Paolo DJ (1988) Neodymium Isotope Geochemistry. Springer-Verlag, Berlin

1005 Di Pisa A, Gattiglio M, Oggiano G (1992) Pre-Hercynian magmatic activity in the nappe
1006 zone (internal and external) of Sardinia: evidence of two within plate basaltic cycles.
1007 In: Carmignani L, Sassi FP (eds) Contribution to the Geology of Italy with special
1008 regards to the Palaeozoic basement. A volume dedicated to Tommaso Cocozza. IGCP
1009 Project 276, Newsletter 5, Siena, pp 33-44
1010 Di Simplicio P, Ferrara G, Ghezzo C, Guasparri G, Pellizzer R, Ricci CA, Rita F,
1011 Sabatini G (1974) II metamorfismo e il magmatismo paleozoico nella Sardegna. Rend
1012 Soc It Mineral Petrol 30:979-1068
1013 Di Vincenzo G, Andriessen PAM, Ghezzo C (1996) Evidence of two different
1014 components in a Hercynian peraluminous cordierite-bearing granite: the San Basilio
1015 intrusion (central Sardinia, Italy). J Petrol 37:1175-1206
1016 Ferré EC, Leake BE (2001). Geodynamic significance of ealy orogenic high-K crustal
1017 and mantle melts: example of the Corsica Batholith. Lithos 59:47-67
1018 Franceschelli M, Gattiglio M, Pannuti F, Fadda S (1992) Illite crystallinity in pelitic
1019 rocks from the external and nappe zone of the Hercynian chain of Sardinia (Italy). In:
1020 Carmigliani L, Sassi FP (eds) Contribution to the Geology of Italy with special regards
1021 to the Palaeozoic basement. A volume dedicated to Tommaso Cocozza. IGCP 276,
1022 Newsletter 5, Siena, pp 127-135
1023 Edel JB (1980) Etude paléomagnétique en Sardaigne - Conséquences pour la
1024 géodynamique de la Méditerranée occidentale. PhD Thesis Université de Strasbourg,
1025 Strasbourg, pp 310
1026 Edel JB, Casini L, Oggiano G, Rossi Ph, Schullmann K (2014) Early Permian 90°
1027 clockwise rotation of the Maures–Estérel–Corsica–Sardinia block confirmed by new

palaeomagnetic data and followed by a Triassic 60° clockwise rotation. Geol Soc Lond Sp Pub 405:333–361

Fedele L, Seghedi I, Chung SL, Laiena F, Lin TH, Morra V, Lustrino M (2016) Post-collisional magmatism in the Late Miocene Rodna-Bârgău district (East Carpathians, Romania): Geochemical constraints and petrogenetic models. Lithos 266-267:367-382

Franceschelli M, Puxeddu M, Cruciani G, Utzeri D (2007) Metabasites with eclogite facies relics from Variscides in Sardinia, Italy: a review. International J Earth Sci 96:795–815

Franciosi L (1999) Petrogenesi dei complessi gabbro-tonalitici tardo-ercinici del Sarrabus meridionale (Sardegna sud-orientale). Unpublished PhD Thesis, University of Catania

Gaeta M, Giuliani A, Perilla S, Misiti V (2013) Reddish metagranites from the Gennargentu igneous complex (Sardinia, Italy): insight into metasomatism induced by magma mingling. J Petrol 54:839-859

Gaggero L, Oggiano G, Buzzi L, Slejko F, Cortesogno F (2007) Post-Variscan mafic dikes from the late orogenic collapse to the Tethyan rift: evidence from Sardinia. Ofioliti 32:15–37

Gébelin A, Roger F, Brunel M (2009) Syntectonic crustal melting and high-grade metamorphism in a transpressional regime, Variscan Massif Central, France. Tectonophysics 477:229–243

Ghezzo C, Orsini JB (1982) Lineamenti strutturali e composizionali del batolite ercinico sardo-corso in Sardegna. In: Carmignani L, Cocozza T, Ghezzo C, Pertusati P, Ricci CA (eds) Guida alla Geologia del Pa1eozoico sardo. Guide Geologiche Regionali. Società Geologica Italiana, pp 165-181

1051 Harrison TM, Watson EB (1984) The behaviour of apatite during crustal anatexis:
1052 equilibrium and kinetic considerations. Geochim Cosmochim Acta 48:1467-1477
1053 Helz RT (1976) Phase relations of basalts in their melting ranges at PH2O = 5 kb. Part II:
1054 Melt compositions. J Petrol 17:139–193
1055 Hoskin PWO, Kinny PD, Wyborn D, Chappell BW (2000) Identifying accessory mineral
1056 saturation during differentiation in granitoid magmas: an integrated approach. J Petrol
1057 41:1365-1396
1058 Kersting AB, Arculus RJ (1994) Klyuchevskoy volcano, Kamchatka, Russia: the role of
1059 high-flux, recharged, tapped and fractionated magma chamber(s) in the genesis of
1060 high-Al_2O_3 from high-MgO basalt. J Petrol 35:1-41.
1061 Irvine T, Baragar W (1971) A guide to the chemical classification of the common
1062 volcanic rocks. Can J Earth Sci 8:523-548
1063 Laporte D, Fernandez A, Orsini JB (1991) Le complexe d'Ile Rousse, Balagne, Corse du
1064 Nord-Ouest: pétrologie et cadre de mise en place des granitoides magnésiopotassiques.
1065 Géol Fr 4:15–30
1066 Leake BE, Woolley AR, Arps CES, Birch WD, Gilbert MC, Grice JD, Hawthorne FC,
1067 Kato A, Kisch HJ, Krivovichev VG, Linthout K, Laird J, Mandarino J, Maresch WV,
1068 Nickel EH, Schumacher JC, Smith DC, Stephenson NCN, Ungaretti L, Whittaker
1069 EJW, Youzhi G (1997) Nomenclature of amphiboles: report of the subcommittee on
1070 amphiboles of the International Mineralogical Association Commission on the New
1071 Minerals and Mineral Names. Mineral Mag 61:295-321
1072 Le Maitre RW (2002) Igneous Rocks: A Classification and Glossary of Terms.
1073 Recommendations of the International Union of Geological Sciences Subcommission

1074 on the Systematics of Igneous Rocks. Cambridge University Press, Cambridge, UK,
1075 pp 256
1076 Martin H, Smithies RH, Rapp R, Moyen J-F, Champion D (2005) An overview of
1077 adakite, tonalite-trondhjemite-granodiorite (TTG), and sanukitoid: relationships and
1078 some implications for crustal evolution. Lithos 79:1-24
1079 Martin H, Moyen J-F, Guitreau M, Blichert-Toft J, Le Pennec J-L (2014) Why Archaean
1080 TTG cannot be generated by MORB melting in subduction zones. Lithos 198-199:1-
1081 13
1082 Matte P (2001) The Variscan collage and orogeny (480–290 Ma) and the tectonic
1083 definition of the Armorica Microplate: a review. Terra Nova 13:122–128
1084 Moyen J-F (2009) High Sr/Y and La/Yb ratios: the meaning of the "adakitic signature".
1085 Lithos 112:556-574
1086 Musumeci G, Spano ME, Cherchi GP, Franceschelli M, Pertusati PC, Cruciani G (2015)
1087 Geological Map of the Monte Grighini Variscan Complex (Sardinia, Italy). J Maps
1088 11:287-298
1089 Naitza S, Conte AM, Cuccuru S, Oggiano G, Secchi F, Tecce F (2017) A Late Variscan
1090 tin province associated to the ilmenite-series granites of the Sardinian Batholith
1091 (Italy): the Sn and Mo mineralisation around the Monte Linas ferroan granite. Ore
1092 Geol Rev 80:1259–1278
1093 Nandedkar RH, Hürlimann N, Ulmer P, Müntener O (2016) Amphibole-melt trace
1094 element partitioning of fractionating calcalkaline magmas in the lower crust: an
1095 experimental study. Contrib Mineral Petrol 171:71 doi:10.1007/s00410-016-1278-0

1096 Nicoletti M, Ardanese LR, Colasante S (1982) La granodiorite di Capo Carbonara
1097 (Sardegna, Italia). Età K-Ar di fasi minerali in paragenesi. Rend Soc Ita Mineral Petrol
1098 38:765-769
1099 Oggiano G, Cherchi GP, Aversano A, Di Pisa A, Ulzega A, Orrù P, Pintus C (2005) Note
1100 illustrative della Carta Geologica d'Italia, Foglio 428 Arzachena. S. EL. CA, Firenze
1101 Oggiano G, Casini L, Mameli P, Rossi P (2007) Long lived dextral strike-slip tectonics in
1102 the southern Variscan Belt: evidence from two syn-kynematic intrusions in north
1103 Sardinia. Geol Fr 2:142
1104 Oggiano G, Gaggero L, Funedda A, Buzzi L, Tiepolo M (2010) Multiple early Paleozoic
1105 volcanic events at the northern Gondwana margin: U–Pb age evidence from the
1106 Southern Variscan branch (Sardinia, Italy). Gondwana Res 17:44–58
1107 Orsini JB (1976) Les granitoides hercyniennes corso-sarde, mise en evidence de deux
1108 associatiòn magmatique. Bull Soc Geol Fr 18:1203-1206
1109 Orsini J-B (1980) Le batholite corso–sarde: un exemple de batholite hercynien (structure,
1110 composition, organisation d'ensemble). Sa place dans la chaîne varisque de l'Europe
1111 moyenne. Unpublished doctoral thesis, Université d'Aix-Marseille III, pp 370
1112 Palin RM, White RW, Green ECR (2016) Partial melting of metabasic rocks and the
1113 generation of tonalitic-trondhjemitic-granodioritic (TTG) crust in the Archaean:
1114 Constraints from phase equilibrium modelling. Precambrian Res 287:73-90
1115 Paquette JL, Ménot R-P, Pin C, Orsini JB (2003) Episodic and short-lived granitic pulses
1116 in a post-collisional setting: evidence from precise U–Pb zircon dating through a
1117 crustal cross-section in Corsica. Chem Geol 198:1–20

1118 Panjasawatwong Y, Danyushevsky LV, Crawford AJ, Harris KL (1997) An experimental
1119 study of the effects of melt composition on plagioclase-melt equilibria at 5 and 10
1120 kbars: implications for the origin of magmatic high-An plagioclase. Contrib Mineral
1121 Petrol 118:420–432
1122 Peccerillo A, Taylor, S.R (1976) Geochemistry of Eocene calc-alkaline volcanic rocks of
1123 the Kastamonu area, northern Turkey. Contrib Mineral Petrol 58:63-81
1124 Petronilho LA (2009) Método Sm-Nd no CPGeo-IGc-USP: procedimentos analíticos
1125 atualmente em rotina. In: Simpósio 45 anos de Geocronologia no Brasil, Boletim de
1126 Resumos Expandidos, 116-118
1127 Pirinu N, Brotzu P, Callegari E, Secchi F (1996) Age and field relationships of albite-rich
1128 monzosyenite intruded into the Sarrabus granitoids (SE Sardinia, Italy). Per Mineral
1129 65:289-304
1130 Plank T (2014) The chemical composition of subducting sediments. Treatise on
1131 Geochemistry 4:607-629
1132 Poli G, Tommasini S (1999) Geochemical modeling of acid-basic magma interaction in
1133 the Sardinia-Corsica Batholith: the case study of Sarrabus, southeastern Sardinia, Italy.
1134 Lithos 46:553-571
1135 Poli G, Ghezzo C, Conticelli S (1989) Geochemistry of granitic rocks from the Hercynian
1136 Sardinia–Corsica Batholith: implication for magma genesis. Lithos 23:247–266
1137 Poli G, Tommasini S, Halliday AN, Manetti P (1994) Evidence of acid-basic magma
1138 interaction processes from the Sardinia Corsica Batholith (Italy). Per Mineral 63:149-
1139 15

1140 Pouchou JL, Pichoir F (1988) A simplified version of the “PAP” model for matrix
1141 corrections in EPMA. In: Newbury DE (ed) Microbeam analysis. San Francisco Press,
1142 San Francisco, pp 315–318
1143 Poza AIM, Druguet E (2016) Structure and tectonic setting of the SE Sardinia mafic dyke
1144 swarm. Insights for the stress state during magma emplacement in the upper crust. J
1145 Geodynamics 101:170–185
1146 Prelević D, Seghedi I (2013) Magmatic response to the post-accretionary orogenesis
1147 within Alpine-Himalayan belt - preface. Lithos 180-181:1-4
1148 Prowatke S, Klemme S (2005) Effect of melt composition on the partitioning of trace
1149 elements between titanite and silicate melt. Geochim Cosmochim Acta 69:695-709
1150 Prowatke S, Klemme S (2006a) Trace element partitioning between apatite and silicate
1151 melts. Geochim Cosmochim Acta 70:4513-4527
1152 Prowatke S, Klemme S (2006b) Rare Earth element partitioning between titanite and
1153 silicate melts: Henry’s Law revisited. Geochim Cosmochim Acta 70:4997-5012
1154 Putirka KD (2008) Thermometers and barometers for volcanic systems. In: Putirka KD,
1155 Tepley F (eds), Minerals, inclusions and volcanic processes. Reviews in Mineralogy
1156 and Geochemistry 69, pp. 61-120
1157 Renna MR, Tribuzio R, Tiepolo M (2006) Interaction between basic and acid magmas
1158 during the latest stages of the post-collisional Variscan evolution: Clues from the
1159 gabbro–granite association of Ota (Corsica–Sardinia batholith). Lithos 92:92-110
1160 Ribeiro JM, Maury RC, Grégoire M (2016) Are adakites slab melts or high-pressure
1161 fractionated mantle melts? J Petrol 57:839-862

1162 Ridolfi F, Renzulli A, Puerini M (2010) Stability and chemical equilibrium of amphibole
1163 in calc-alkaline magmas: an overview, new thermobarometric formulations and
1164 application to subduction-related volcanoes. Contrib Mineral Petrol 160:45-66
1165 Roeder PL, Emslie RF (1970) Olivine-liquid equilibrium. Contrib Mineral Petrol 29:275–
1166 289
1167 Ronca S, Del Moro A, Traversa G (1999) Geochronology, Sr-Nd isotope geochemistry
1168 and petrology of Late Hercynian dike magmatism from Sarrabus (SE Sardinia). Per
1169 Mineral 68:231–260
1170 Rossi, Ph., Cocherie, A., 1991. Genesis of a Variscan batholith: field, petrological and
1171 mineralogical evidence from the Corsica-Sardinia batholith. Tectonophysics 195, 319–
1172 346.
1173 Rossi P, Chavez JY, Cocherie A (1988) Age varisque précoce du plutonisme magnésio
1174 potassique en Corse occidentale: conséquences géodynamiques. C R Acad Sci
1175 307:1541–1547
1176 Rossi Ph, Oggiano G, Cocherie A (2009) A restored section of the "southern Variscan
1177 realm" across the Corsica–Sardinia microcontinent. C R Geosci 341:224–238
1178 Rossi Ph, Cocherie A, Fanning CM (2015) Evidence in Variscan Corsica of a brief and
1179 voluminous Late Carboniferous to Early Permian volcanic-plutonic event
1180 contemporaneous with a high-temperature/low-pressure metamorphic peak in the
1181 lower crust. Bull Soc Geol Fr 186:171–192
1182 Scaillet B, Holtz F, Pichavant M (1998) Phase equilibrium constraints on the viscosity of
1183 silicic magmas 1. Volcanic-plutonic comparison. J Geophys Res 103:27257-27266

1184 Scaillet B, Evans BWE (1999) The 15 June 1991 eruption of Mount Pinatubo. I. Phase
1185 equilibria and pre-eruption P-T-fO_2-fH_2O conditions of the dacite magma. J Petrol
1186 40:381-411
1187 Secchi F, D'Antonio M (1996) Inferences of Sr, Nd and O isotopic tracers on the origin
1188 and evolution of a gabbronorite-granodiorite sequence from southern Hercynian chain
1189 of Sardinia. A case study from the Arburése igneous complex and its comparison with
1190 the earlier sequences of Sàrrabus area. Per Mineral 65:257–273
1191 Secchi F, Brotzu P, Callegari E (1991) The Arburese igneous complex: an example of
1192 igneous fractionation leading to peraluminous granites as residual melts. Chem Geol
1193 92:213–249
1194 Secchi F, Cincotti F, Cherchi GP, Sarria E (2001) Geological and petrographical aspects
1195 of late Hercynian intrusive sequences from southern Ogliastra area (SE Sardinia,
1196 Italy). Per Mineral 70:303-332
1197 Shaw J, Johnston ST (2016) Oroclinal buckling of the Armorican ribbon continent: an
1198 alternative tectonic model for Pangean amalgamation and Variscan orogenesis.
1199 Lithosphere 8:769–777
1200 Sisson TW, Grove TL (1993) Experimental investigations of the role of H_2O in calc-
1201 alkaline differentiation and subduction zone magmatism. Contrib Mineral Petrol
1202 113:143–166
1203 Stormer JC, Nicholls J (1978) XLFRAC: a program for interactive testing of magmatic
1204 differentiation
1205 models. Comp Geosci 4:143–159
1206 Streckeisen A (1976) To each plutonic rock its proper name. Earth Sci Rev 12:1-33

1207 Souza SL (2009) Métodos radiométricos Rb-Sr e Sm-Nd no CPGeo-IGc-USP. In:
1208 Simpósio 45 anos de Geocronologia no Brasil, Boletim de Resumos Expandidos, 137-
1209 139
1210 Spulber SD, Rutherford MJ (1983) The origin of rhyolite and plagiogranite in oceanic
1211 crust: an experimental study. J Petrol 24:1–25
1212 Taylor RJM, Harley SL, Hinton RW, Elphick S, Clark C, Kelly NM (2015) Experimental
1213 determination of REE partition coefficients between zircon, garnet and melt: a key to
1214 understanding high-T crustal processes. J Metamorph Geol 33:231-248
1215 Tommasini S, Poli G (1992) Petrology of the late-Carboniferous Punta Falcone gabbroic
1216 complex, northern Sardinia, Italy. Contrib Mineral Petrol 110:16-32
1217 Tommasini S, Poli G, Halliday AN (1995) The role of sediment subduction and crustal
1218 growth in Hercynian plutonism: isotopic and trace element evidence from the Sardinia
1219 Corsica Batholith. J Petrol 36:1305-1332
1220 Tommasini S, Poli G, Ghezzo C (1999) Trace element inferences on the evolution and
1221 genesis of the Monte Pulchiana leucogranites, northern Sardinia, Italy. Per Mineral
1222 68:53-67
1223 Wang K-L, Chung S-L, O'Reilly SY, Sun S-S, Shinjo R, Chen C-H (2004) Geochemical
1224 constraints for the genesis of post-collisional magmatism and the geodynamic
1225 evolution of the Northern Taiwan Region. J Petrol 45:975-1011
1226 Wang M, Song S, Niu Y, Su L (2014) Post-collisional magmatism: consequences of
1227 UHPM terrane exhumation and orogen collapse, N. Qaidam UHPM belt, NW China.
1228 Lithos 210-211:181-198

Watson EB, Harrison TM (1983) Zircon saturation revisited: temperature and compositional effects in a variety of crustal magma types. Earth Planet Sci Lett 64:295-304

Wolf MB, Wyllie PJ (1994) Dehydration-melting of amphibolite at 10 kbar; the effects of temperature and time. Contrib Mineral Petrol 115:369–383

Zorpi MJ, Coulon C, Orsini J-B, Cocirta C (1989) Magma mingling, zoning and emplacement in calc-alkaline granitoid plutons. Tectonophysics 157:315–329

Zorpi MJ, Coulon C, Orsini J-B (1991) Hybridization between felsic and mafic magmas in calc-alkaline granitoids; a case study in northern Sardinia, Italy. Chem Geol 92:45–86

Figure captions

Fig. 1. Simplified geological sketch maps of a) Sardinia Basement (after Carmignani et al. 2015), b) southern Sàrrabus pluton (after Poza and Druguet, 2016) and c) of the Solanas complex (after Franciosi, 1999), with location of the investigated samples.

Fig. 2. Representative field photographs showing the relationships between microgabbros and tonalitic-granodioritic rocks in the Solanas complex. a) Stretched microgranular mafic enclave in amphibole granodiorite (south of Porto Murroni); b) contacts between microgabbro and tonalite along the Cagliari-Villasimius main road. Subangular to slightly rounded fragments of microgabbro dispersed in tonalitic/quartz-dioritic rocks; c) Blobs of microgranular gabbro in tonalitic/quartz-dioritic rock forming a “pillow-like” structure. Large crystals of plagioclase and minor amounts of quartz, biotite and amphibole from host rock, giving to the microgabbros a “porphyritic-like” appearance; d)

1252 detailed view of c) showing the plagioclase xenocrysts from tonalitic/quartz-dioritic rocks
1253 dispersed in the microgabbro.
1254 **Fig. 3.** Modal composition of Solanas rock samples reported in the Q-A-P classification
1255 diagram (Streckeisen, 1976).
1256 **Fig. 4.** Representative photomicrographs (crossed polarizers view) of the investigated
1257 rock samples from the Solanas complex. a) Olivine gabbronorite (sample GRL36) with
1258 olivine, orthopyroxene, clinopyroxene and plagioclase grains enclosed in large amphibole
1259 oikocryst; b) amphibole gabbro (sample GRL35) showing large complex-zoned
1260 plagioclase crystals; c) microgabbro (sample L31) with plagioclase, amphibole, biotite
1261 and small interstitial quartz grains; d) porphyritic-like microgabbro (sample L11)
1262 showing a resorbed and zoned plagioclase xenocryst; e) quartz-diorite (sample L14)
1263 showing euhedral biotite within large amphibole oikocryst; f) plagiogranite (sample L55)
1264 with plagioclase, quartz, biotite, amphibole and orthopyroxene; g) amphibole
1265 granodiorite (sample GRL41) with plagioclase, quartz, alkali feldspar, amphibole and
1266 biotite; h) biotite granodiorite (sample GRL10) with plagioclase, quartz, alkali-feldspar
1267 and biotite.
1268 **Fig. 5**. a) 100*Mg# in olivine vs. 100*Mg# in whole-rock for the Solanas olivine
1269 gabbronorites. Lines for K_d^{Mg-Fe}=0.30±0.03 (Roeder and Emslie 1970) that reflect
1270 olivine-liquid equilibrium are shown. b) Composition of the pyroxene crystals from the
1271 Solanas rocks. The data for the pyroxenes from the Burcei gabbroic rocks (Brotzu et al.
1272 1993) are also shown. c) Composition of the amphibole crystals from the Solanas rocks
1273 in the classification diagram of Leake et al. (1997).

Fig. 6. a) Composition of plagioclase and alkali feldspar crystals from the Solanas rocks; b) Composition of mica crystals from the Solanas rocks in the classification diagram of Deer et al. (1992). ^{VI}Al in atoms per formula unit.

Fig. 7. a) Total Alkali vs. SiO_2 (TAS; Le Maitre 2002) and b) K_2O vs. SiO_2 (Peccerillo and Taylor 1976) classification diagrams for the investigated rock samples from the Solanas complex. The dashed line in a) separates the fields for subalkaline and alkaline rock series [according to Irvine and Baragar (1971)]. The data for the gabbroic rocks from Capo Carbonara (Sàrrabus; Poli and Tommasini 1999), Punta Falcone (northern Sardinia batholith; Tommasini and Poli 1992) and Burcei (Sàrrabus; Brotzu et al. 1993), and for the basic/intermediate dykes crosscutting the Sàrrabus pluton (Ronca et al. 1999) are also reported for comparison.

Fig. 8. Selected major elements vs. MgO binary diagrams for the investigated rock samples from the Solanas complex, together with data for the gabbroic rocks from Capo Carbonara (Sàrrabus), Punta Falcone (northern Sardinia batholith) and Burcei (Sàrrabus), and for the basic/intermediate dykes crosscutting the Sàrrabus pluton. Symbols and data sources as in Fig. 7.

Fig. 9. Selected trace elements vs. MgO binary diagrams for the investigated rock samples from the Solanas complex, together with data for the gabbroic rocks from Capo Carbonara (Sàrrabus), Punta Falcone (northern Sardinia batholith) and Burcei (Sàrrabus), and for the basic/intermediate dykes crosscutting the Sàrrabus pluton. Symbols and data sources as in Fig. 7.

Fig. 10. Chondrite-normalized (Sun and McDonough 1989) multi-element diagrams for the investigated a) olivine gabbronorite (oGb), amphibole gabbro (aGb) and microgabbro

(mGb), b) quartz diorite (QD) and tonalite (TN), c) plagiogranite (plG), amphibole-granodiorite (aGd) and biotite-granodiorite (btGd) rock samples from the Solanas complex and for d) the gabbroic rocks from Capo Carbonara (Sàrrabus), e) Punta Falcone (northern Sardinia batholith) and e) Burcei (Sàrrabus) and the dykes crosscutting the Sàrrabus pluton.

Fig. 11. Primitive mantle-normalized (Sun and McDonough 1989) multi-element diagrams for the investigated a) olivine gabbronorite (oGb), amphibole gabbro (aGb) and microgabbro (mGb), b) quartz diorite (QD) and tonalite (TN), c) plagiogranite (plG), amphibole-granodiorite (aGd) and biotite-granodiorite (btGd) rock samples from the Solanas complex and for d) the gabbroic rocks from Capo Carbonara (Sàrrabus), e) Punta Falcone (northern Sardinia batholith) and e) Burcei (Sàrrabus) and the dykes crosscutting the Sàrrabus pluton. The pattern for the estimated composition of global subducted sediments (GLOSS-2; Plank 2014) is reported for comparison.

Fig. 12. a) $(^{87}Sr/^{86}Sr)_i$ vs. MgO, b) $(^{143}Nd/^{144}Nd)_i$ vs. MgO and c) $(^{143}Nd/^{144}Nd)_i$ vs. $(^{87}Sr/^{86}Sr)_i$ diagrams for the investigated rock samples from the Solanas complex, together with data for the gabbroic rocks from Capo Carbonara (Sàrrabus), Punta Falcone (northern Sardinia batholith) and Burcei (Sàrrabus), for the basic/intermediate dykes crosscutting the Sàrrabus pluton and for the other rocks of the Sardinia-Corsica batholith (black triangles; Secchi et al. 1991, 2001; Tommasini et al. 1995, 1999; Di Vincenzo et al. 1996; Barbey et al. 2008; Gaeta et al. 2013; Conte et al. 2017). Isotopic ratios were calculated back to 300 Ma based on the estimated emplacement ages for the Sàrrabus pluton reported by Nicoletti et al. (1982) and here. Symbols and data sources as in Fig. 7.

Fig. 13. a) Anorthite content in plagioclase vs. Fo content in olivine for the Solanas oGb. The arc gabbros and oceanic cumulates fields are after Beard (1986). b) Anorthite content in plagioclase vs. Mg# of clinopyroxene for Solanas oGb. Fields for MORB and arc gabbros are from Burns (1985).

Fig. 14. a) Sr/Y vs. Y and b) La/Yb vs. Yb (after Castillo 2012) and c) La_N/Yb_N vs. Yb_N (after Ribeiro et al. 2016) diagrams for the investigated intermediate and evolved rock samples from the Solanas complex. ADR = normal arc andesite, dacite and rhyolite lavas.

Table captions

Table 1. Major- (in wt.%) and trace element (in ppm) XRF data and loss on ignition values (LOI, in wt.%) for the investigated rock samples from the Solanas complex.

oGb = olivine gabbronorite; aGb = amphibole gabbro; mGb = microgabbro; QD = quartz diorite; T = tonalite; plG = plagiogranite; aGd = amphibole-grandiorite; btGd = biotite-granodiorite.

b.d.l. = below detection limits

Table 2. Trace element (in ppm) ICP-MS data and Sr-Nd isotope ratios [meas = measured; in = initial, age-corrected to 300 Ma] for the investigated rock samples from the Solanas complex.

Supplementary Tables

Table S1: Summary of the main textural and mineralogical features of the recognized lithotypes from the Solanas complex.

Table S2-9: Mineral chemistry data. Table S2: Olivine; Table S3: Pyroxenes; Table S4: Spinels; Table S5: Fe-Ti oxides; Table S6: Amphiboles; Table S7: Feldspars; Table S8: Mica; Table S9: Apatite; Table S10: Titanite and zircon.

Table S11: Results of mass balance calculations.

Table S12: Analyses of certified materials.

Table S13: Analyses of international standards (whole-rock).

Supplementary Figures

Figure S1: Back-scattered electron (BSE) images for some representative plagioclase crystals from the Solanas rocks, with schematic sketch and corresponding An profiles measured by SEM-EDS. a) Plagioclase from aGb sample GRL35, showing complex patchy-zoned texture; b) plagioclase from mGb sample L11, showing resorption of the grain interior; c) Plagioclase from mGb sample L71, showing complex patchy zoned texture.

Figure S2: Rb-Sr isochron diagram for the QD sample GRL16. The isochron was obtained using data from whole rock, biotite and amphibole separates.

Figure S3: Chondrite-normalized (Sun and McDonough 1989) multi-element diagrams with the results of fractional crystallisation models starting from TN (sample L33), QD (L57) and aGd (L13) magma compositions. Calculated liquid compositions (liq. calc.) match well with the rock compositions for samples L81 (btGd) and L55 (plG). Bulk distribution coefficients (D) have been estimated using the proportions of minerals in the fractional crystallization extracts (obtained from mass balance calculations) in

combination with mineral-liquid distribution coefficients from the literature (GERM website; http://www.earthref.org).

Figure S4: Comparison of Solanas rock compositions with those of experimental liquids produced by partial melting of hydrated basaltic rocks, greenstones, and amphibolites. Fields enclose the experimental data of Wolf and Wyllie (1994), Beard and Lofgren (1991), Spulberg and Rutherford (1983) and Helz (1976). Symbols and data sources as in Fig. 7.

Fig.1

Click here to access/download;Figure;Sarrabus-Solanas Fig1.tif

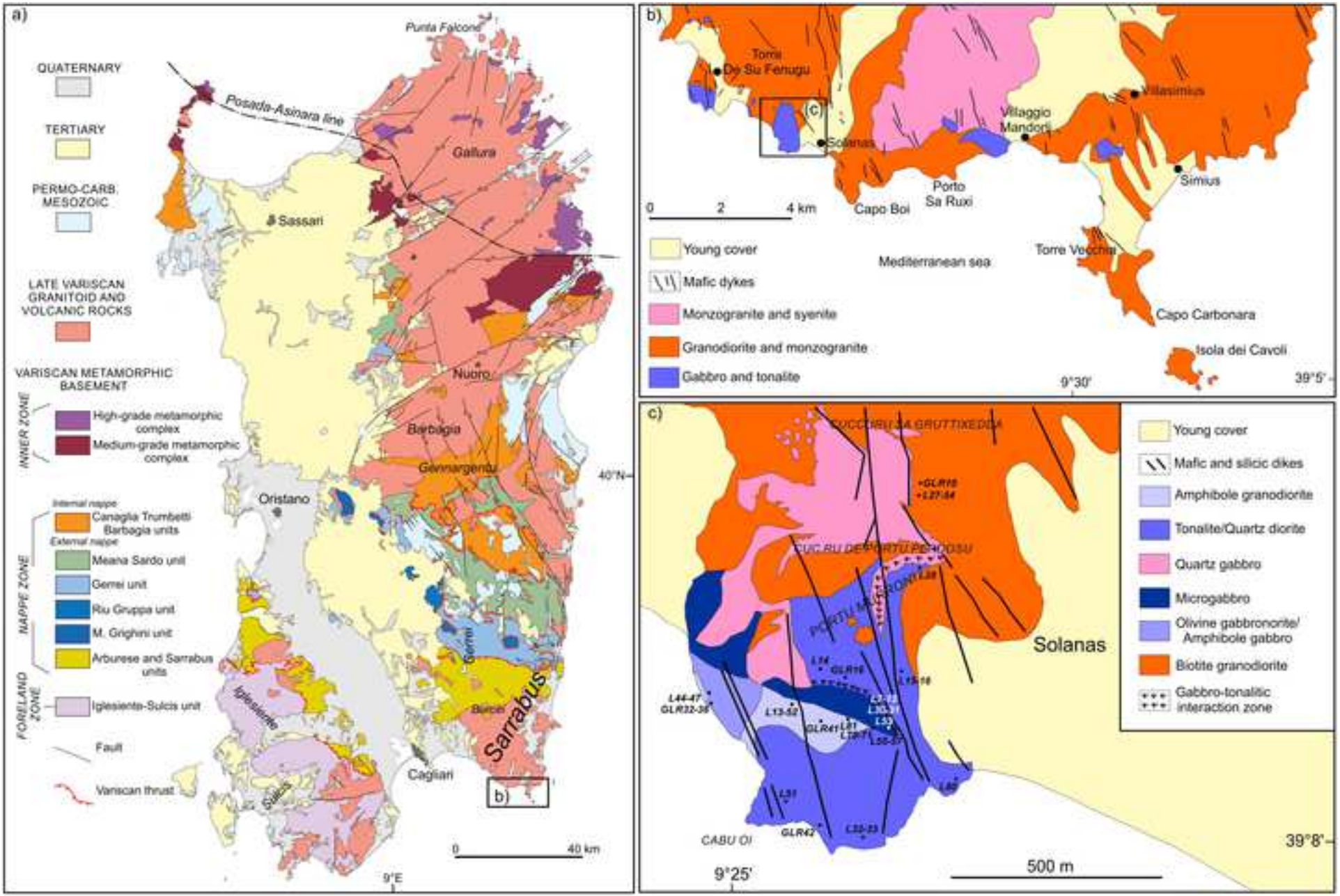

Fig.2

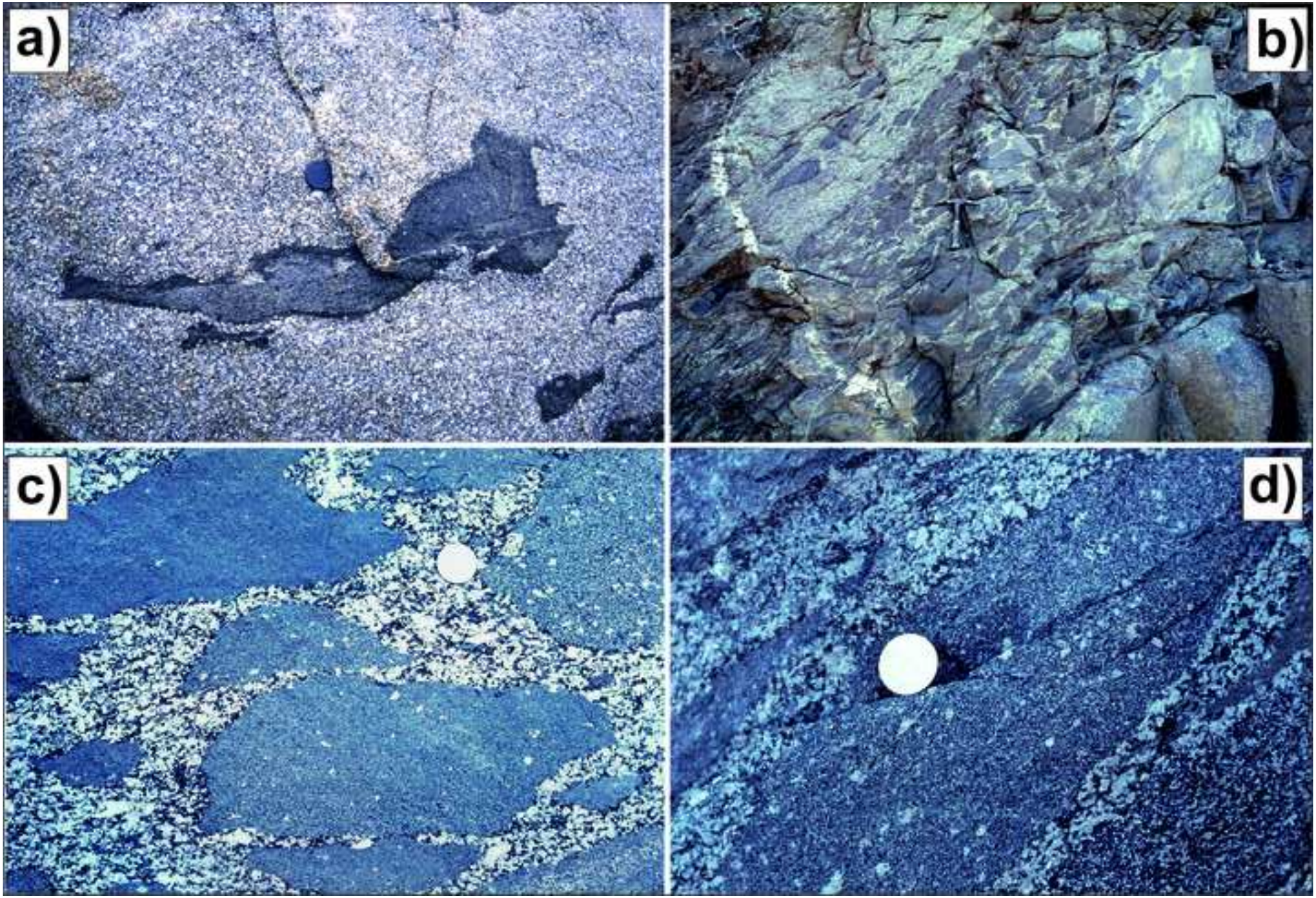

Fig.3

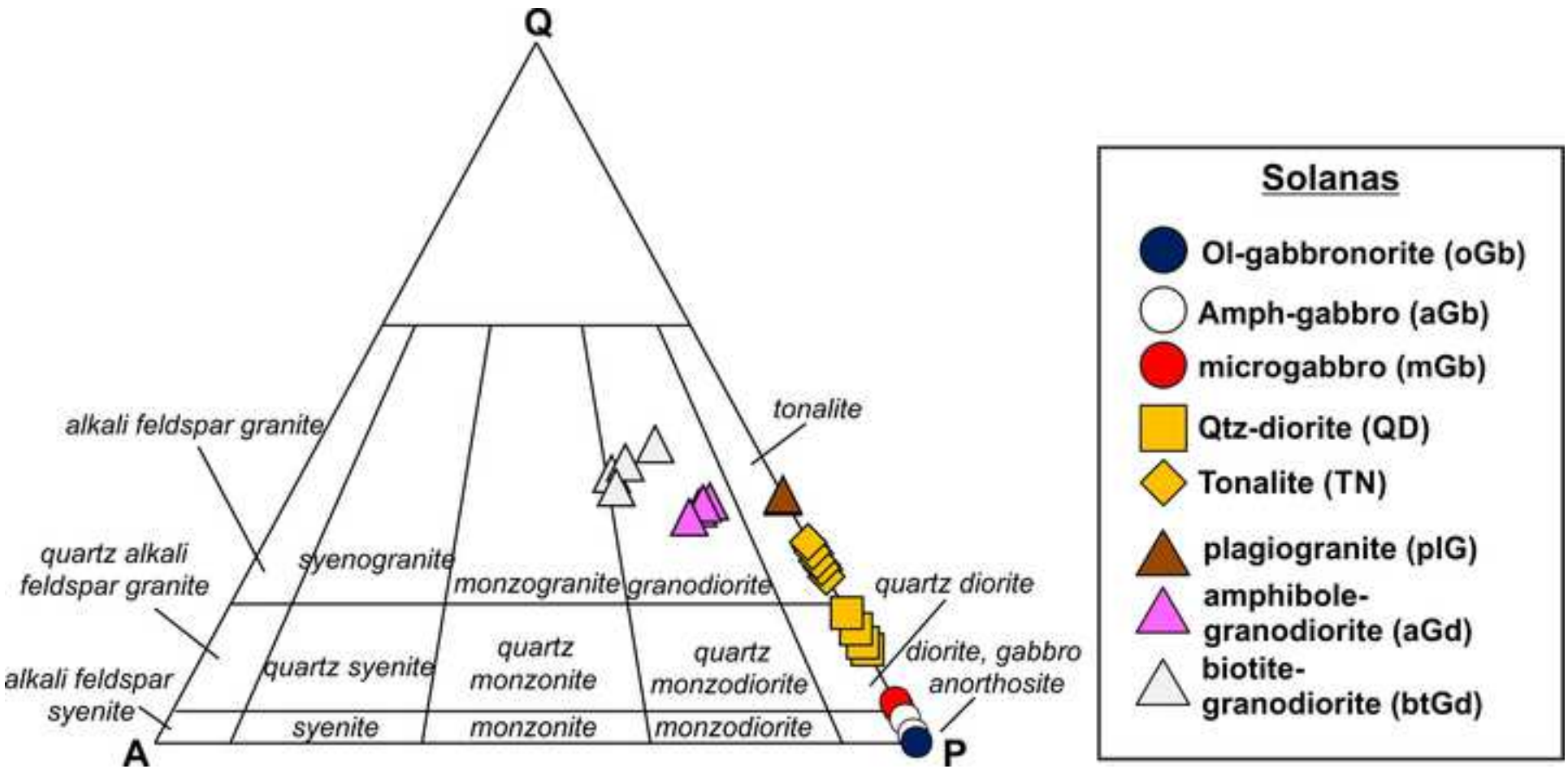

Fig.4 Click here to access/download;Figure;Sarrabus-Solanas Fig4.tif

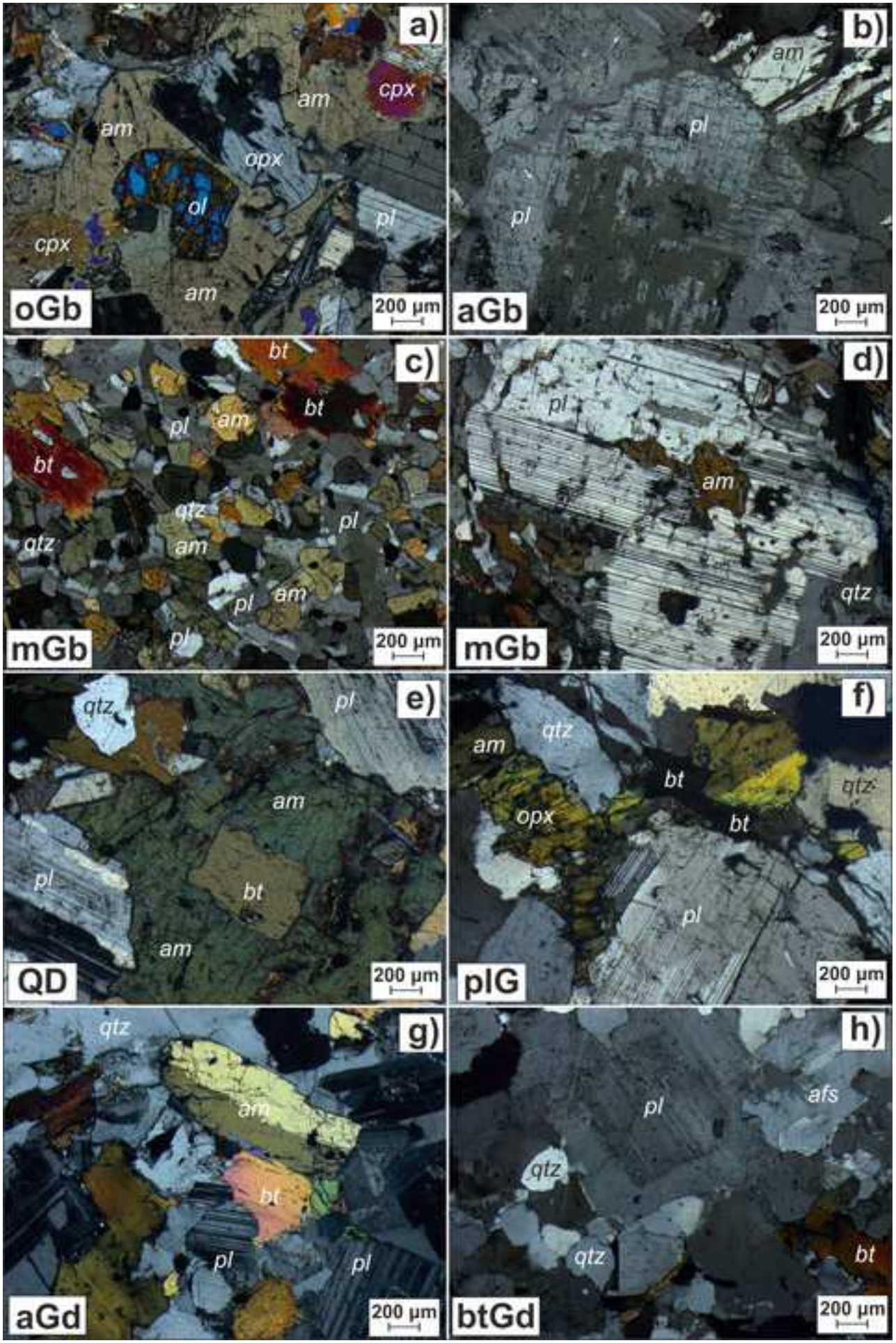

Fig.5

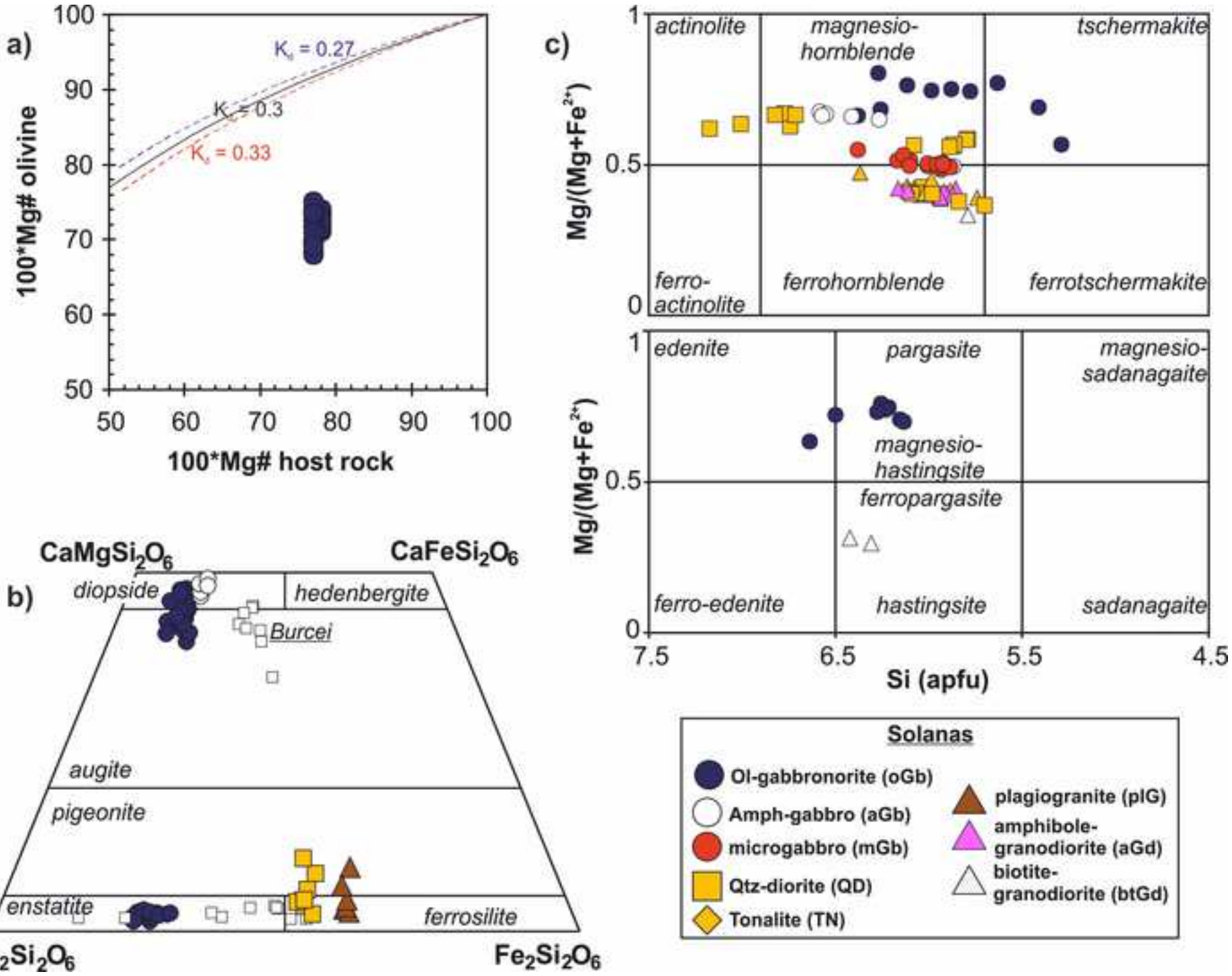

Fig.6

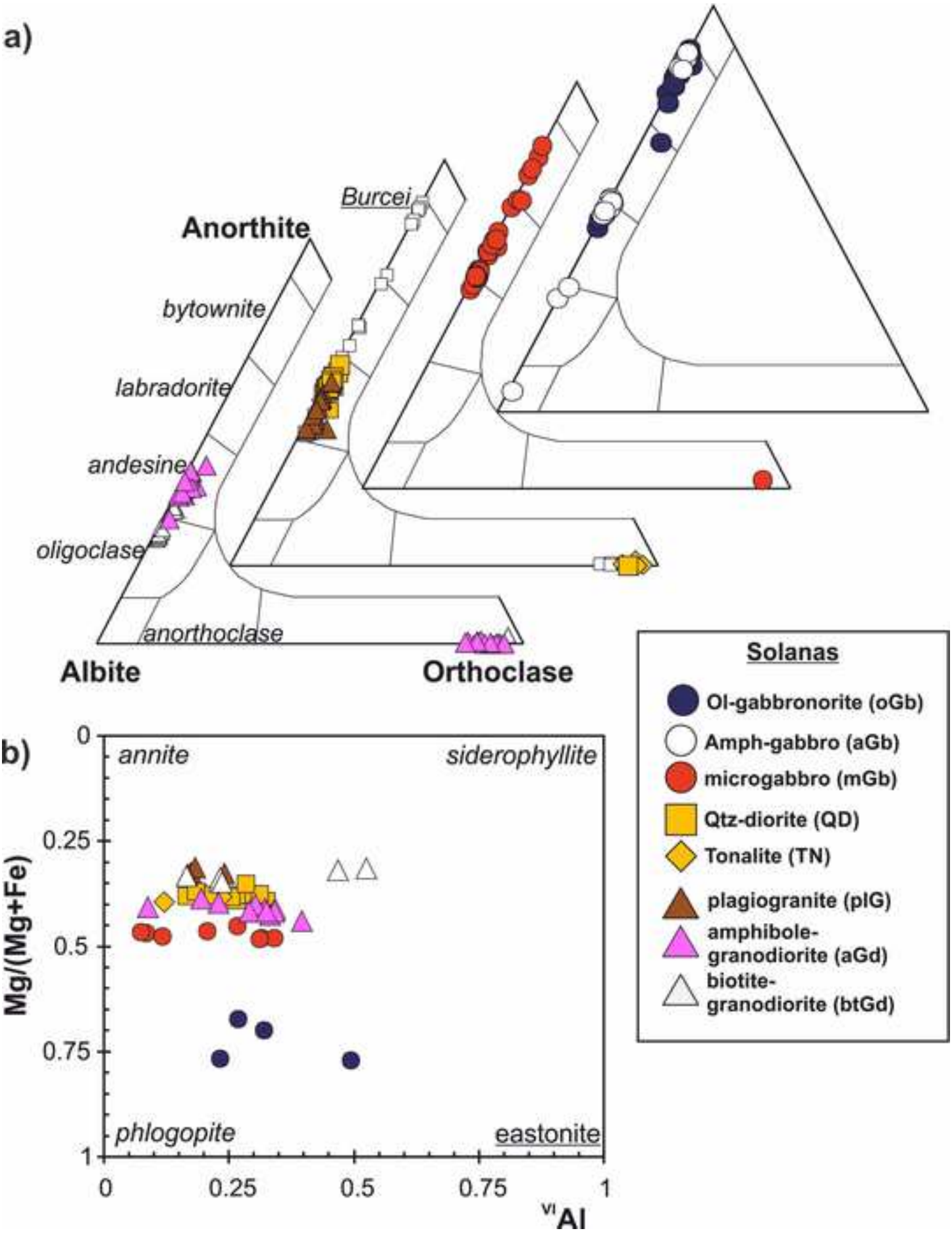

Fig.7

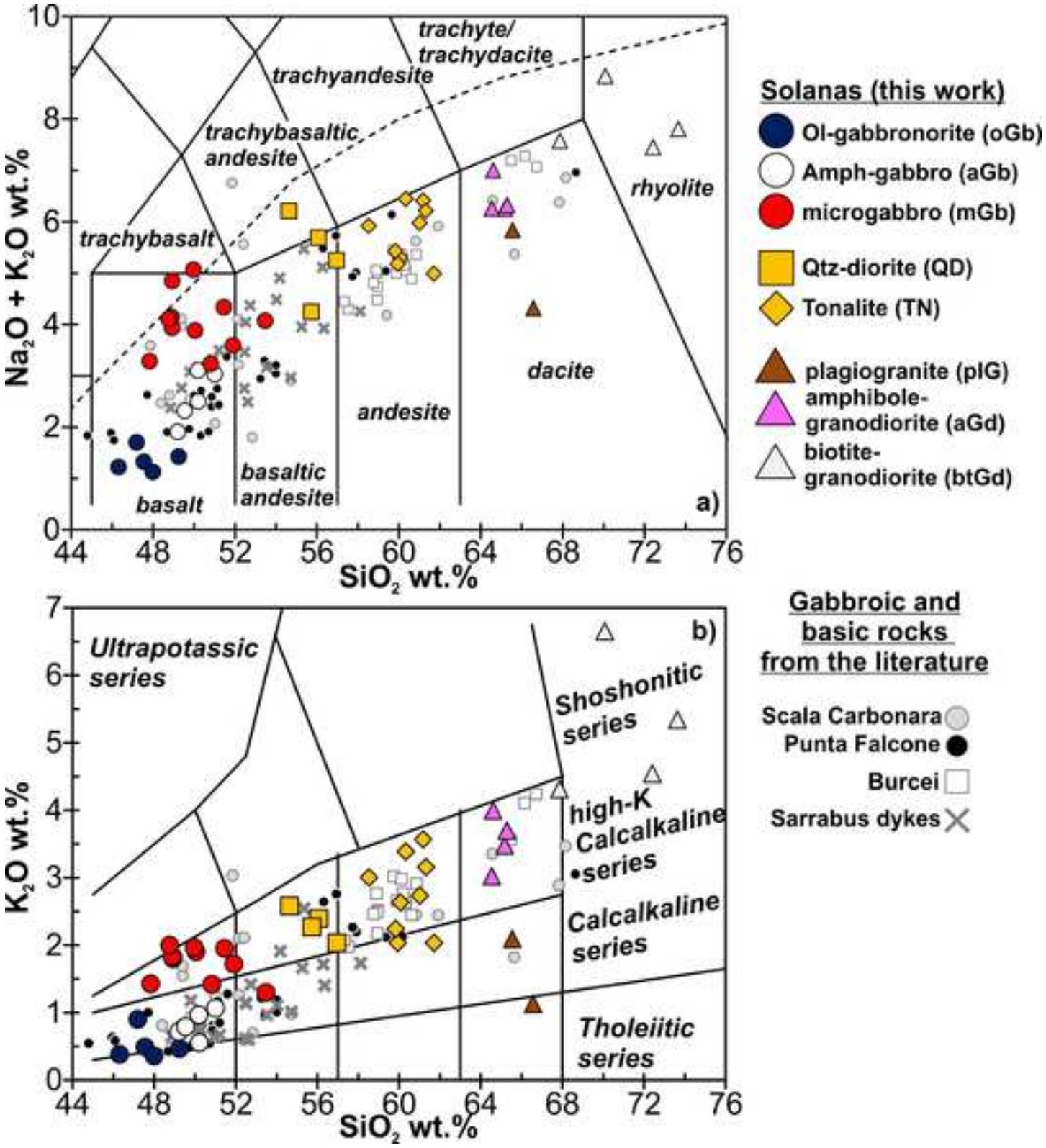

Fig.8

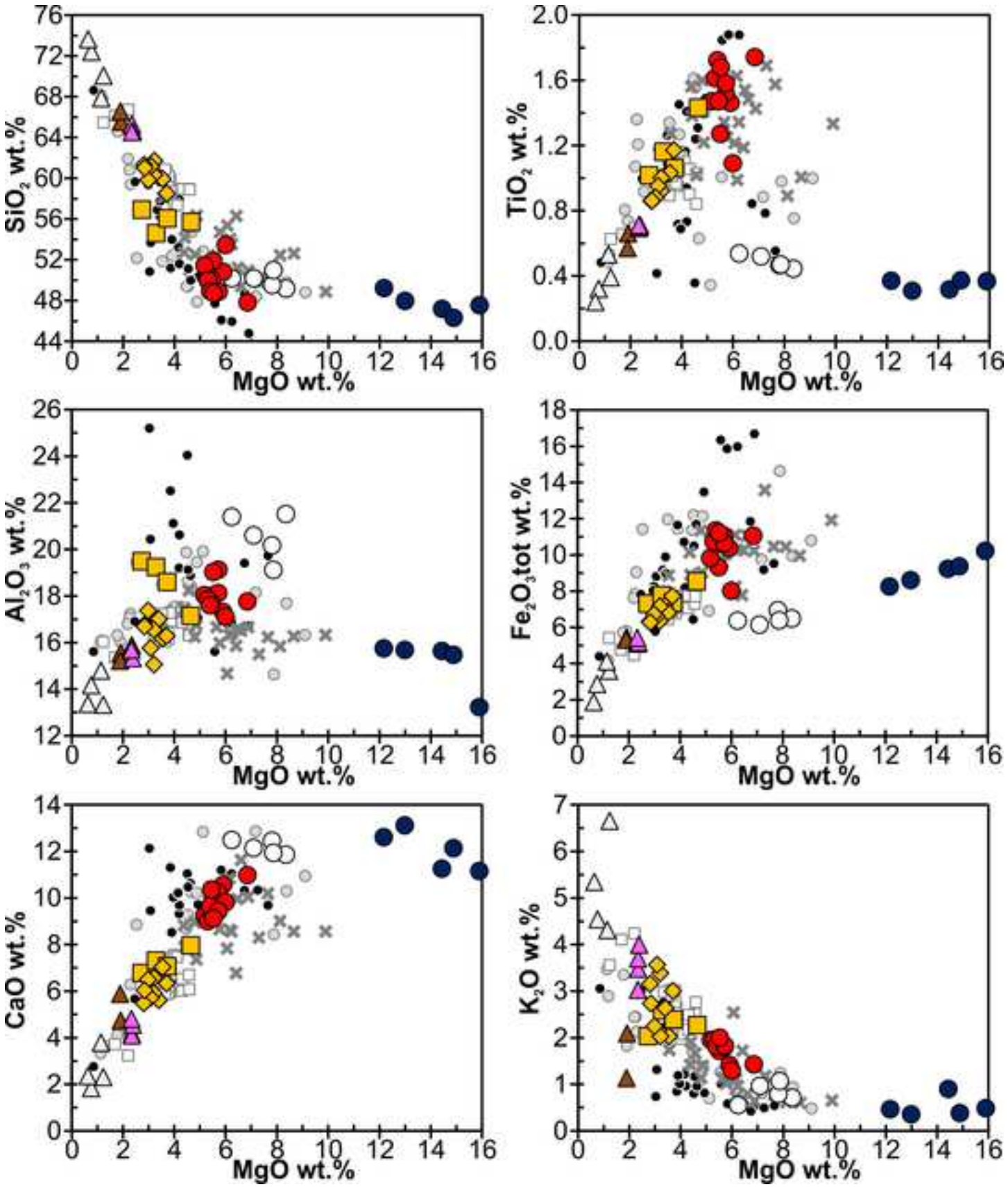

Fig.9

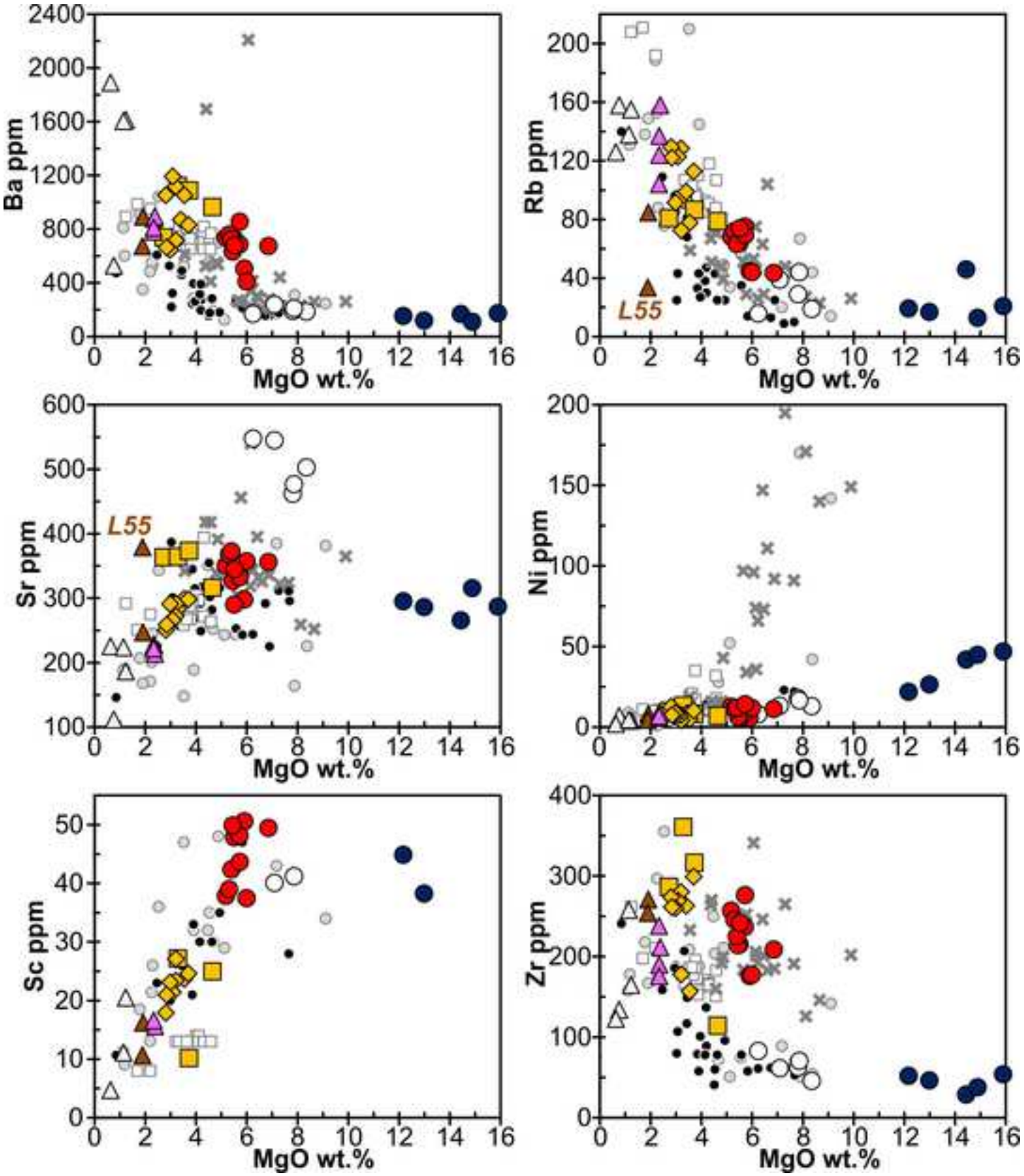

Fig.10

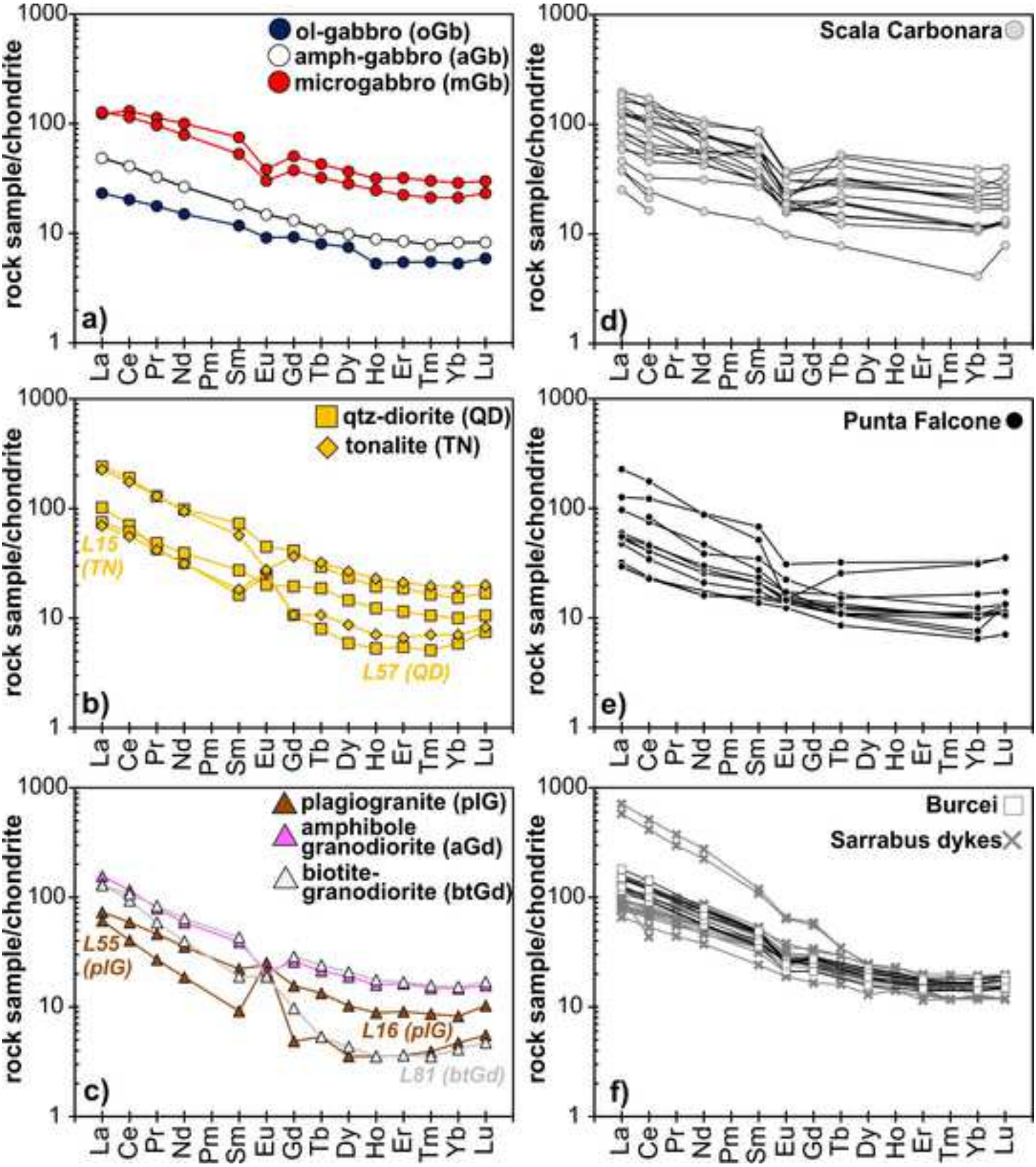

Fig.11

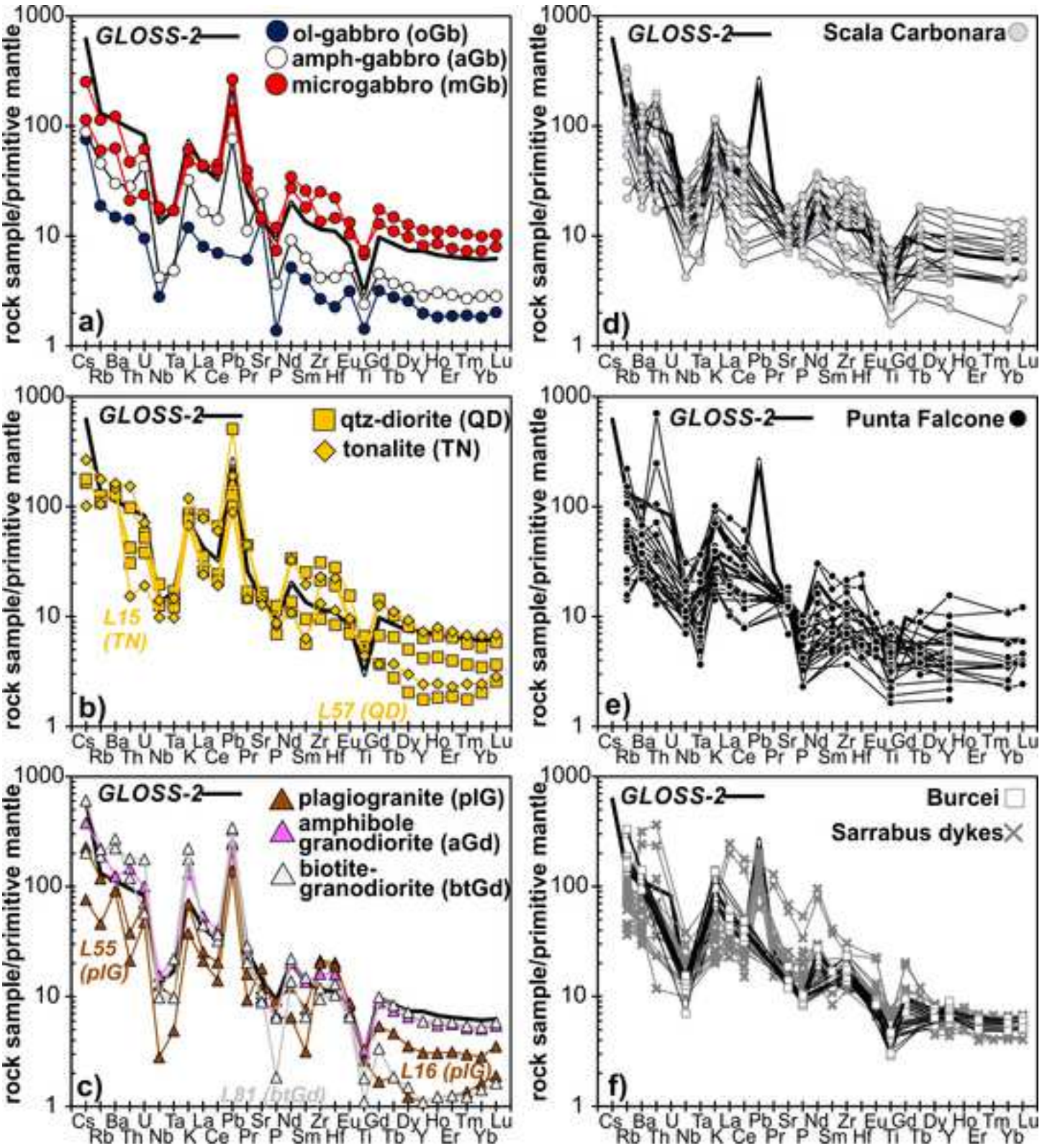

Fig.12

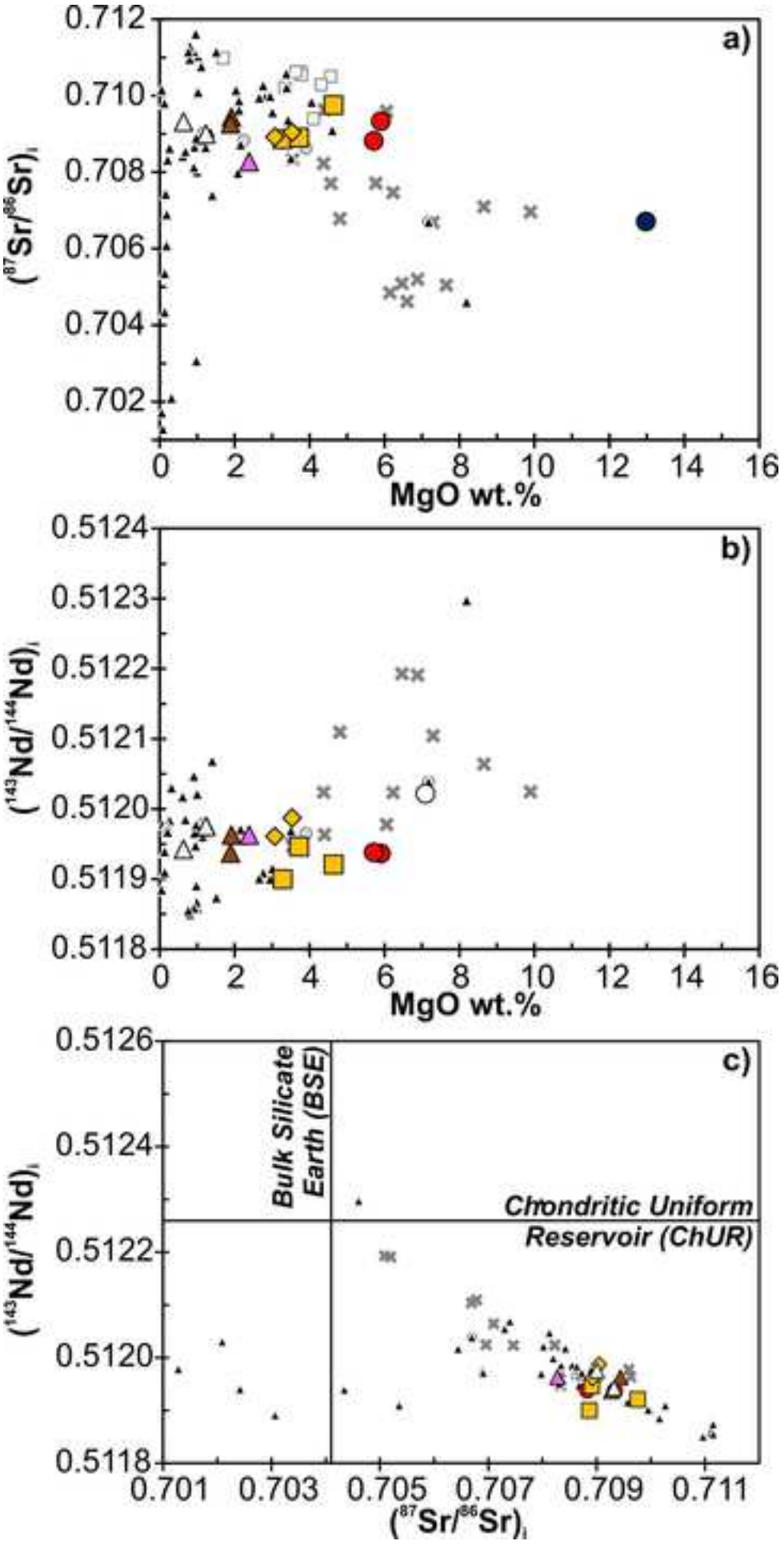

Fig.13

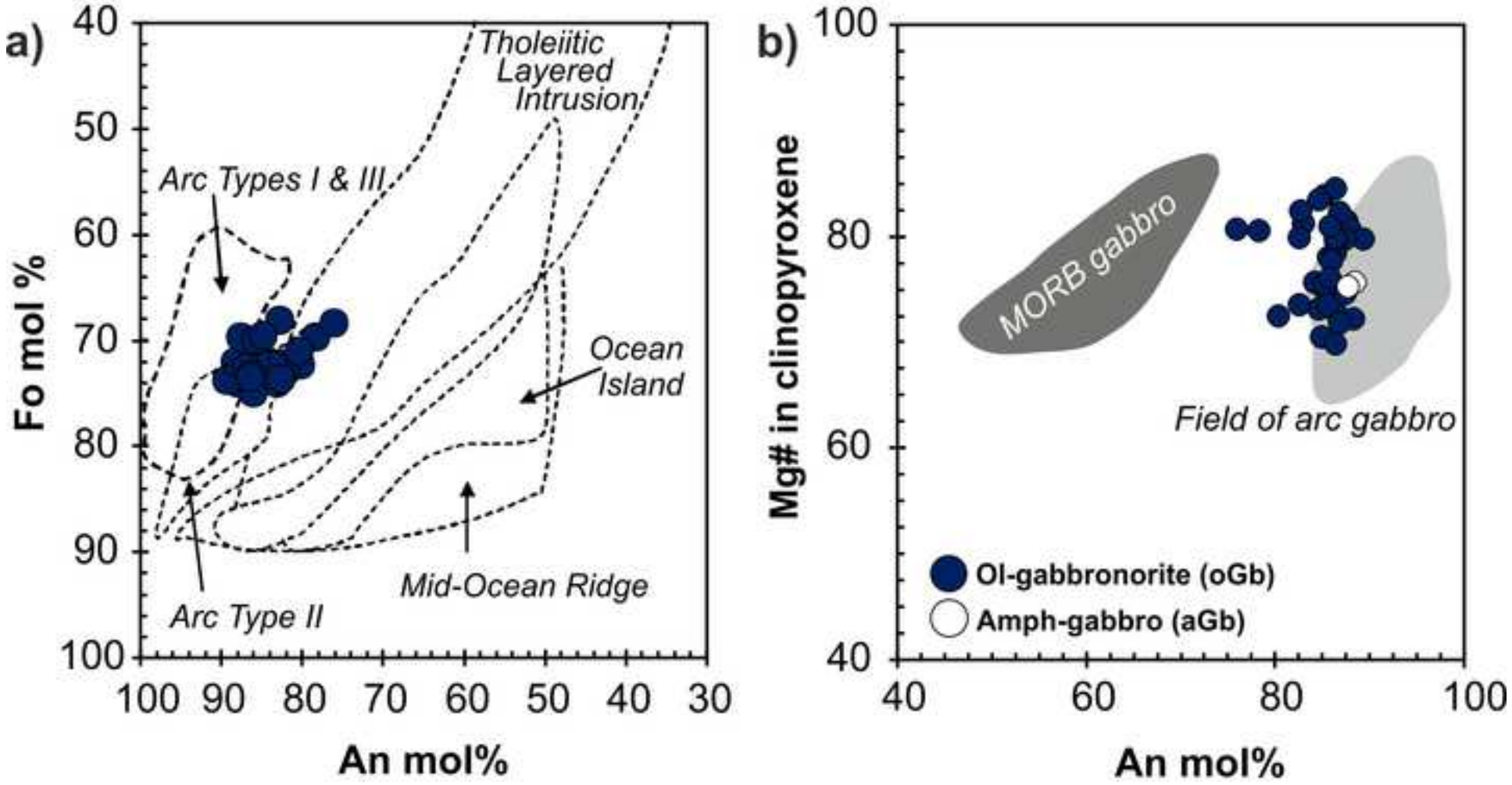

Fig.14

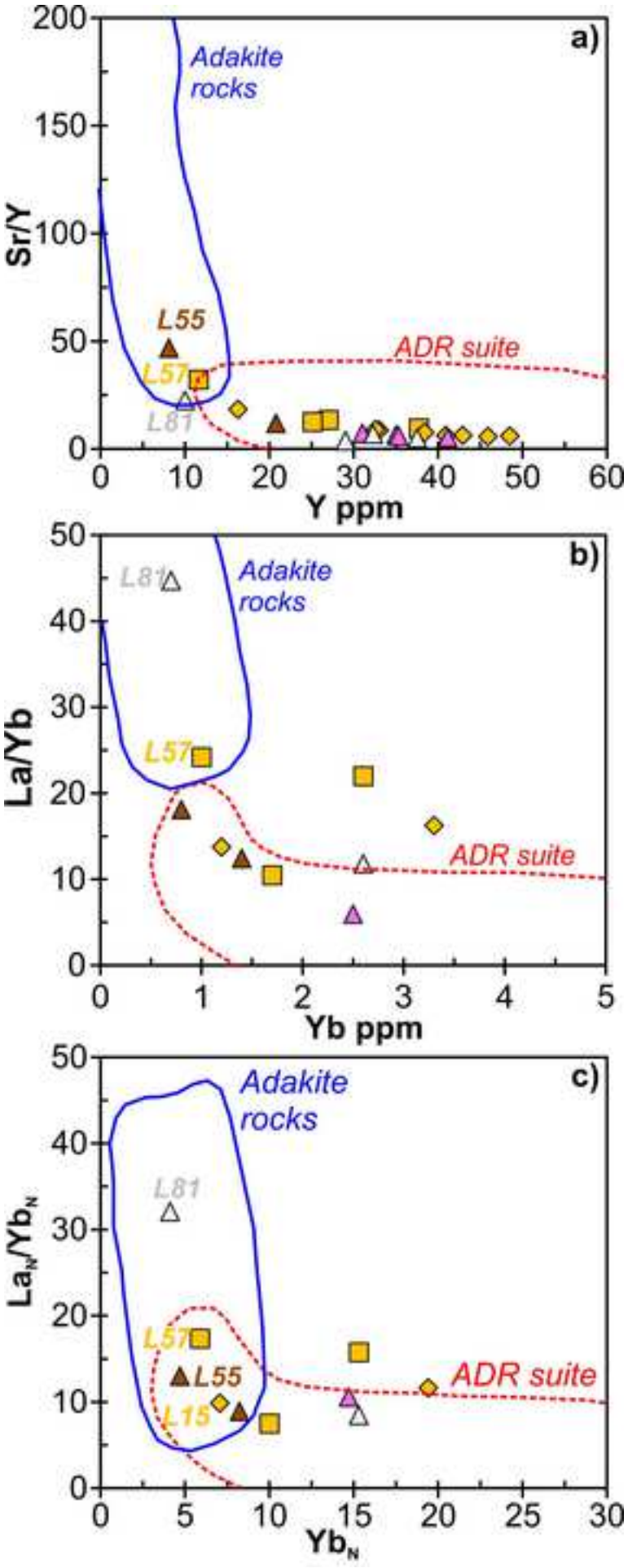

Table 1

Table 1: Major- (in wt.%) and trace element (in ppm) XRF data and loss on ignition values (LOI, in wt.%) for the investigated rock samples from the Solanas complex

sample	rock name	location	SiO_2	TiO_2	Al_2O_3	Fe_2O_{3t}	MnO	MgO	CaO	Na_2O	K_2O	P_2O_5	LOI	Rb	Sr	Y	Zr	Nb	Ba	Cr	Ni	Sc	V	La	Ce
GLR33	oGb	Cabu Oi	47.54	0.37	13.23	10.23	0.16	15.89	11.16	0.84	0.49	0.08	2.92	21	287	4	54	b.d.l.	175	820	47	b.d.l.	138	6.0	18.0
GLR34	oGb	Cabu Oi	47.19	0.32	15.64	9.24	0.15	14.43	11.27	0.80	0.90	0.06	3.45	46	266	b.d.l.	29	b.d.l.	169	658	42	b.d.l.	113	2.0	17.0
GLR36	oGb	Cabu Oi	46.30	0.37	15.48	9.39	0.14	14.88	12.15	0.84	0.38	0.06	1.77	13	316	b.d.l.	38	b.d.l.	111	625	45	b.d.l.	123	8.0	12.0
L45	oGb	Cabu Oi	47.98	0.31	15.69	8.62	0.13	12.98	13.13	0.77	0.36	0.03	1.23	17	286	12	47	3	121	494	27	38	106	0.6	7.7
L46	oGb	Cabu Oi	49.23	0.37	15.75	8.26	0.14	12.16	12.62	0.96	0.47	0.04	1.01	19	296	14	52	3	156	465	22	45	122	4.3	7.8
GLR35	aGb	Cabu Oi	50.20	0.54	21.41	6.39	0.11	6.24	12.49	1.95	0.56	0.12	1.83	16	548	5	83	b.d.l.	169	75	8	b.d.l.	157	12.0	14.0
GLR37	aGb	Cabu Oi	49.20	0.45	21.53	6.49	0.12	8.35	11.87	1.19	0.72	0.09	1.55	19	503	b.d.l.	46	b.d.l.	186	114	13	b.d.l.	118	7.0	11.0
GLR38	aGb	Cabu Oi	49.53	0.47	20.18	6.96	0.12	7.81	12.46	1.53	0.79	0.15	1.81	29	462	4	63	b.d.l.	192	240	18	b.d.l.	122	14.0	35.0
L44	aGb	Cabu Oi	50.19	0.52	20.61	6.16	0.10	7.09	12.16	2.13	0.97	0.08	2.34	39	545	15	62	b.d.l.	239	93	13	40	172	0.1	16.1
L47	aGb	Cabu Oi	51.00	0.47	19.12	6.40	0.11	7.86	11.94	1.96	1.07	0.07	2.68	44	477	17	71	b.d.l.	212	240	17	41	138	10.2	18.1
L7	mGb	C.P.P.	50.82	1.46	17.32	10.39	0.16	5.90	10.57	1.81	1.42	0.16	0.87	45	298	62	176	15	508	30	6	51	286	27.0	63.6
L8	mGb	C.P.P.	51.89	1.27	18.02	9.32	0.14	5.50	10.07	1.87	1.72	0.19	0.80	64	290	57	215	12	730	21	6	48	234	17.5	44.9
L10	mGb	C.P.P.	48.92	1.52	18.13	11.06	0.18	5.71	10.26	2.13	1.80	0.28	2.34	75	337	66	237	16	688	25	9	48	273	23.2	74.6
L11	mGb	C.P.P.	51.44	1.47	18.04	9.84	0.16	5.17	9.25	2.38	1.95	0.29	1.05	68	351	46	257	15	738	36	13	38	219	27.4	56.0
L12	mGb	C.P.P.	50.05	1.47	17.74	10.61	0.16	5.44	10.37	1.98	1.90	0.28	1.23	70	327	62	214	15	635	27	6	50	223	20.3	65.5
L30	mGb	C.P.P.	49.96	1.61	17.85	10.75	0.16	5.30	9.01	3.11	1.96	0.29	1.51	72	368	55	246	13	761	25	11	39	236	29.7	68.8
L31	mGb	C.P.P.	48.92	1.72	17.60	11.36	0.18	5.39	9.65	3.03	1.82	0.32	1.07	63	373	62	225	14	724	33	12	42	283	23.8	68.6
L53	mGb	C.P.P.	47.83	1.74	17.77	11.07	0.17	6.84	10.99	1.85	1.43	0.30	1.00	44	356	55	209	12	675	61	11	50	265	15.8	65.2
L71	mGb	C.P.P.	48.88	1.58	19.13	10.66	0.17	5.71	9.45	2.32	1.83	0.26	0.83	69	333	50	276	14	857	29	14	44	251	29.2	56.9
GLR16	QD	P.M.	56.94	1.02	19.50	7.32	0.11	2.72	6.78	3.22	2.04	0.35	1.42	81	364	27	287	11	740	b.d.l.	10	b.d.l.	136	38.0	70.0
L14	QD	P.M.	54.63	1.16	19.24	7.79	0.12	3.28	7.32	3.63	2.59	0.25	0.74	94	365	38	361	14	1123	24	14	27	126	47.0	81.1
L57	QD	C.P.P.	56.07	1.06	18.61	7.38	0.12	3.72	7.08	3.30	2.40	0.27	0.58	87	374	12	317	7	1089	28	8	10	117	18.7	17.2
L70	QD	C.P.P.	55.72	1.43	17.15	8.56	0.13	4.64	7.97	1.97	2.27	0.15	0.73	79	317	25	114	13	966	24	7	25	197	13.7	21.4
GLR42	TN	P.M.	60.06	1.02	17.01	7.20	0.11	3.40	5.61	2.66	2.63	0.28	1.78	99	288	33	263	12	870	b.d.l.	8	b.d.l.	131	41.0	66.0
L15	TN	C.P.P.	59.94	1.03	16.18	6.82	0.10	3.54	7.03	3.15	2.03	0.18	0.86	78	299	16	157	11	1053	21	5	24	208	13.8	21.7
L28	TN	C.P.P.	61.71	1.00	15.06	7.16	0.11	3.21	6.57	2.95	2.03	0.19	0.56	73	292	49	178	15	718	11	4	27	180	19.2	55.9
L32	TN	P.M.	60.33	0.92	16.55	6.35	0.09	3.20	5.91	3.06	3.39	0.20	0.71	129	272	43	280	16	1117	22	8	23	134	62.0	94.2
L33	TN	P.M.	61.18	0.95	15.76	6.60	0.10	3.08	5.71	2.85	3.57	0.19	0.66	123	266	46	269	16	1194	38	8	21	126	49.7	80.7
L51	TN	P.M.	61.31	0.86	16.74	6.31	0.09	2.81	5.48	3.06	3.16	0.18	0.75	130	251	41	274	15	1053	21	13	18	152	43.9	109.5
L79	TN	P.M.	59.83	0.88	17.37	6.72	0.10	2.98	6.49	3.19	2.24	0.20	0.69	92	291	33	260	13	646	31	9	23	129	34.4	67.2
L80	TN	P.M.	61.01	0.86	16.70	6.29	0.10	2.84	6.04	3.24	2.73	0.18	0.81	122	259	41	261	17	664	26	8	21	119	27.7	57.9
L91	TN	C.P.P.	58.53	1.17	16.28	7.73	0.12	3.70	6.33	2.92	3.01	0.22	0.39	113	298	38	299	17	833	33	10	25	107	24.4	63.0
L16	plG	C.P.P.	65.55	0.66	15.56	5.44	0.10	1.91	4.74	3.75	2.09	0.20	0.74	85	247	21	271	15	892	9	8	16	85	9.5	29.3
L55	plG	C.P.P.	66.56	0.57	15.21	5.33	0.10	1.89	5.88	3.18	1.13	0.14	0.71	34	379	8	254	3	673	17	5	11	96	4.9	14.1
GLR32	aGd	Cabu Oi	65.17	0.69	15.88	5.20	0.08	2.34	4.18	2.77	3.48	0.20	0.90	124	228	31	190	6	878	b.d.l.	6	b.d.l.	94	54.0	79.0
GLR41	aGd	P.M.	65.28	0.70	15.83	5.11	0.09	2.34	4.09	2.63	3.70	0.22	0.91	137	227	35	176	6	782	b.d.l.	9	b.d.l.	87	47.0	75.0
L13	aGd	P.M.	64.60	0.71	15.33	5.18	0.08	2.38	4.56	3.01	4.00	0.15	0.56	158	214	35	212	15	895	29	8	16	117	33.3	55.5
L52	aGd	P.M.	64.54	0.71	15.69	5.42	0.09	2.33	4.81	3.24	3.03	0.15	1.68	104	222	41	238	16	811	17	7	17	121	47.0	87.4
GLR10	btGd	P.M.	72.41	0.32	14.17	2.87	0.05	0.76	1.84	2.91	4.54	0.13	0.52	158	112	29	134	11	528	b.d.l.	7	b.d.l.	33	12.0	33.0
L27	btGd	P.M.	70.08	0.39	13.33	3.61	0.06	1.23	2.32	2.19	6.66	0.14	0.61	155	187	38	165	16	1614	b.d.l.	4	21	80	38.0	57.4
L81	btGd	P.M.	73.64	0.24	13.36	1.88	0.03	0.63	2.36	2.47	5.34	0.04	0.55	126	225	10	123	8	1891	6	2	5	114	30.0	41.1
L54	btGd	P.M.	67.86	0.53	14.80	4.12	0.06	1.14	3.79	3.27	4.31	0.12	0.52	138	224	32	258	15	1604	b.d.l.	5	11	80	57.5	84.8

oGb = olivine gabbronorite; aGb = amphibole gabbro; mGb = microgabbro; QD = quartz diorite; T = tonalite; plG = plagiogranite; aGd = amphibole-grandiorite; btGd = biotite-granodiorite.
b.d.l. = below detection limits
C.P.P. = Cuccuru de Portu Perdosu; P.M. = Porto Murroni

Table 2

Table 2: Trace element (in ppm) ICP-MS data and Sr-Nd isotope ratios for the investigated rock samples from the Solanas complex

sample	L45	L44	L7	L71	L14	L57	L70	L15	L33	L16	L55	L13	L27	L81
rock name	oGb	aGb	mGb	mGb	QD	QD	QD	TN	TN	plG	plG	aGd	btGd	btGd
location	Cabu Oi	Cabu Oi	C.P.P.	C.P.P.	P.M.	C.P.P.	C.P.P.	C.P.P.	P.M.	C.P.P.	C.P.P.	P.M.	P.M.	P.M.
Sc	36	30	44	36	21	6	24	22	19	10	6	13	17	2
Be	b.d.l.	b.d.l.	1	1	2	2	b.d.l.	2	2	2	1	2	2	2
V	120	150	298	272	131	117	207	178	116	66	85	88	39	24
Ba	104	210	440	854	921	1021	891	1021	1129	874	638	864	1564	1893
Sr	295	516	290	313	327	347	320	302	270	251	379	204	188	225
Y	9	13	51	37	29	8	19	11	33	14	5	27	27	5
Zr	30	47	152	283	347	237	107	147	256	238	227	180	133	106
Cr	440	80	40	20	30	b.d.l.	b.d.l.	b.d.l.	30	b.d.l.	b.d.l.	b.d.l.	b.d.l.	b.d.l.
Co	49	19	21	21	12	15	17	10	11	7	7	9	5	2
Ni	30	b.d.l.	b.d.l.	20	b.d.l.	b.d.l.	b.d.l.	b.d.l.	b.d.l.	b.d.l.	b.d.l.	b.d.l.	b.d.l.	b.d.l.
Cu	20	b.d.l.	20	10	50	b.d.l.	b.d.l.	20	b.d.l.	b.d.l.	b.d.l.	b.d.l.	b.d.l.	b.d.l.
Zn	70	50	110	170	100	100	130	90	90	80	70	70	50	b.d.l.
Ga	13	18	22	23	26	23	20	20	22	20	18	20	16	15
Ge	2.0	2.0	3.0	2.0	2.0	2.0	2.0	2.0	2.0	2.0	1.0	2.0	2.0	1.0
Rb	12	29	38	72	78	80	69	67	112	75	29	141	138	120
Nb	2.0	3.0	12.0	13.0	14.0	9.0	9.0	7.0	10.0	9.0	2.0	11.0	7.0	7.0
Ag	b.d.l.	0.6	1.3	2.2	2.8	1.1	0.9	1.1	2.1	1.7	1.8	0.8	1.3	0.6
Sn	b.d.l.	1.0	1.0	1.0	1.0	b.d.l.	b.d.l.	b.d.l.	1.0	b.d.l.	b.d.l.	2.0	1.0	b.d.l.
Cs	0.6	0.7	0.9	2.0	1.3	1.3	1.4	0.8	2.1	1.8	0.6	3.0	4.8	1.6
La	5.5	11.5	29.2	30.2	57.2	24.2	17.8	16.5	53.6	17.4	14.5	36.9	30.7	31.3
Ce	12.4	25.1	79.8	70.3	117.0	43.1	37.4	34.0	107.0	36.1	24.8	71.2	65.4	57.3
Pr	1.7	3.1	10.8	9.2	12.3	4.1	4.6	4.0	12.4	4.4	2.6	7.5	8.0	5.6
Nd	7.0	12.4	46.8	36.9	45.8	14.9	18.4	14.6	44.2	16.5	8.7	27.6	30.0	18.6
Sm	1.8	2.8	11.5	8.1	11.2	2.5	4.2	2.8	8.7	3.4	1.4	6.0	6.6	2.9
Eu	0.5	0.9	2.2	1.8	2.6	1.4	1.2	1.5	1.6	1.4	1.5	1.2	1.1	1.1
Gd	1.90	2.70	10.40	7.70	8.50	2.20	4.00	2.20	7.50	3.20	1.00	5.30	5.90	2.00
Tb	0.30	0.40	1.60	1.20	1.10	0.30	0.70	0.40	1.20	0.50	0.20	0.80	0.90	0.20
Dy	1.90	2.50	9.30	7.20	6.00	1.50	3.70	2.20	6.80	2.60	0.90	4.80	5.30	1.10
Ho	0.30	0.50	1.80	1.40	1.10	0.30	0.70	0.40	1.30	0.50	0.20	0.90	1.00	0.20
Er	0.90	1.40	5.30	3.70	3.10	0.90	1.90	1.10	3.50	1.50	0.60	2.70	2.80	0.60
Tm	0.14	0.20	0.77	0.54	0.42	0.13	0.27	0.18	0.50	0.22	0.10	0.38	0.40	0.09
Yb	0.90	1.40	4.90	3.60	2.60	1.00	1.70	1.20	3.30	1.40	0.80	2.50	2.60	0.70
Lu	0.15	0.21	0.76	0.59	0.43	0.19	0.27	0.21	0.51	0.26	0.14	0.40	0.43	0.12
Hf	0.70	1.30	4.50	6.90	8.60	5.90	2.60	3.50	6.90	6.30	5.80	4.90	4.00	3.20
Ta	b.d.l.	0.20	0.70	0.70	0.70	0.50	0.60	0.40	0.60	0.40	0.20	0.90	0.90	0.40
Tl	0.60	0.30	0.20	0.40	0.40	0.40	0.30	0.30	0.50	0.40	0.20	0.70	0.60	0.50
Pb	b.d.l.	6.00	21.00	11.00	40.00	11.00	10.00	7.00	15.00	19.00	11.00	20.00	27.00	26.00
Th	1.20	2.40	1.80	4.00	8.30	2.60	3.60	1.30	13.00	3.20	1.80	12.40	15.30	10.20
U	0.20	0.90	0.50	1.30	1.20	1.10	0.80	0.40	1.50	1.50	1.00	2.10	3.70	1.20
$^{87}Rb/^{86}Sr$	0.118	-	0.379	0.666	0.691	0.668	0.624	0.642	1.201	0.865	0.222	2.002	2.127	1.545
$^{87}Sr/^{86}Sr_m$	0.70722	-	0.71094	0.71165	0.71179	0.71174	0.71241	0.71177	0.71402	0.71310	0.71021	0.71676	0.71802	0.71587
± 2s	0.00004	-	0.00004	0.00005	0.00004	0.00005	0.00005	0.00004	0.00004	0.00004	0.00005	0.00004	0.00005	0.00005
$^{87}Sr/^{86}Sr_i$	0.70672	-	0.70933	0.70882	0.70886	0.70891	0.70976	0.70905	0.70892	0.70944	0.70927	0.70827	0.70900	0.70932
$^{147}Sm/^{144}Nd$		0.137	0.149	0.133	0.148	0.101	0.138	0.116	0.119	0.125	0.097	0.131	0.133	0.094
$^{143}Nd/^{144}Nd_m$	-	0.512288	0.512227	0.512197	0.512189	0.512144	0.512190	0.512213	0.512193	0.512206	0.512127	0.512219	0.512235	0.512126
± 2s	-	0.000007	0.000005	0.000006	0.000006	0.000007	0.000007	0.000008	0.000007	0.000006	0.000006	0.000006	0.000005	0.000007
$^{143}Nd/^{144}Nd_i$	-	0.512020	0.511940	0.511940	0.511900	0.511950	0.511920	0.511990	0.511960	0.511960	0.511940	0.511960	0.511980	0.511940
εNd_m	-	-6.9	-8.1	-8.6	-8.8	-9.7	-8.8	-8.3	-8.7	-8.5	-10.0	-8.2	-7.9	-10.0
εNd_i	-	-4.6	-6.2	-6.2	-7.0	-6.0	-6.5	-5.3	-5.8	-5.7	-6.2	-5.7	-5.5	-6.1
T_{DM} (Ga)	-	1.19	1.44	1.27	1.49	1.05	1.35	1.08	1.14	1.17	1.04	1.23	1.22	1.02

oGb = olivine gabbronorite; aGb = amphibole gabbro; mGb = microgabbro; QD = quartz diorite; T = tonalite; plG = plagiogranite; aGd = amphibole-grandiorite; btGd = biotite-granodiorite.

Sr and Nd isotopic analyses were normalised to $^{88}Sr/^{86}Sr = 0.1194$ and $^{146}Nd/^{144}Nd = 0.7219$, respectively. εNd values have been calculated for the rocks using a chondritic average value of $^{143}Nd/^{144}Nd = 0.512638$ and $^{147}Sm/^{144}Nd = 0.1967$. Initial isotopic ratios have been calculated at 300 Ma (meas = measured; in = initial).

T_{DM}, refer to one-stage model age (De Paolo, 1981; 1988); b.d.l. = below detection limits; C.P.P. = Cuccuru de Portu Perdosu; P.M. = Porto Murroni

Electronic Supplementary Material Fig.1

Electronic Supplementary Material Fig.2

Electronic Supplementary Material Fig.4

Electronic Supplementary Material suppl. Tables

Click here to access/download

Electronic Supplementary Material

Sarrabus-Solanas supplementary Tables.xls